



Time-Dependent Radiation Quality Factor $\langle Q \rangle$ of Galactic Cosmic Rays in Deep Space and Shielding Environments: Modeling and Measurements

Weihaio Liu^{a,b,*}, Mikhail Dobynde^{b,*}, Jingnan Guo^{b,**}, Jordanka Semkova^c,
Krasimir Krastev^c, Cary Zeitlin^d

^aDepartment of Climate and Space Sciences and Engineering, University of Michigan, Ann Arbor, MI 48109, USA

^bNational Key Laboratory of Deep Space Exploration/School of Earth and Space Sciences, University of Science and Technology of China, Hefei 230026, People's Republic of China

^cSpace Research and Technology Institute, Bulgarian Academy of Science, Sofia 1113, Bulgaria

^dLeidos Inc., Houston, TX 77042, USA

Abstract

Understanding the long-term variation of the galactic cosmic ray (GCR) radiation environment is critical for assessing radiation risks in space exploration missions. In this study, we systematically model the linear energy transfer (LET) spectra of GCRs and the corresponding radiation quality factor, $\langle Q \rangle$, in deep space and shielding environments. The Badhwar–O’Neill 2020 (BON20) model is used to represent GCR fluxes under different solar modulation potentials (ϕ), which characterize the level of solar activity. GCR interactions with spherical shielding of different thicknesses are simulated to obtain the LET spectra, absorbed dose, dose equivalent, and $\langle Q \rangle$. We present a comprehensive dataset of these quantities for a range of ϕ values and shielding thicknesses. The results show that $\langle Q \rangle$ depends strongly on the shielding thickness but only weakly on solar activity. Furthermore, model predictions are validated against long-term measurements from the Cosmic Ray Telescope for the Effects of Radiation (CRaTER) orbiting the Moon, as well as the Liulin-MO detector on board the ExoMars Trace Gas Orbiter (TGO) orbiting Mars. In this comparison, we account for factors for anomalous cosmic ray (ACR) contributions and the radial gradients of both GCRs and ACRs, applying scaling factors of 6.3% at 1 AU and 11.0% at 1.5 AU to the calculated absorbed dose rate. With these corrections included, the modeled absorbed dose rate and $\langle Q \rangle$ exhibit consistent temporal variations with the observations under both thin and thick shielding conditions. Moreover, we investigate the distinct temporal evolution of $\langle Q \rangle$ for light and heavy GCR nuclei, revealing how solar modulation influences the elemental radiation quality factor across GCR species. These results offer new insights into the temporal and environmental dependence of the space radiation quality factor, with implications for radiation dose estimate and crewed mission design.

© 2011 Published by Elsevier Ltd.

Keywords: Galactic cosmic rays, Linear energy transfer, Radiation quality factor, Radiation transport modeling

*These authors contribute equally to this work.

**Corresponding author

Email address: jnguo@ustc.edu.cn (Jingnan Guo)

1. Introduction

Deep space exploration has been a central focus of space agencies worldwide for decades. Space radiation, however, can present severe risks not only for the operational lifespan of satellites and the performance of onboard instruments but also for the health of astronauts (Zheng et al., 2019; Jun et al., 2024). In the heliosphere, the radiation environment is mainly composed of the background galactic cosmic rays (GCRs), anomalous cosmic rays (ACRs) and occasional solar energetic particle (SEP) events (e.g., Kudela, 2009; Guo et al., 2024). GCRs are the slowly varying background energetic particles that originate outside the solar system. In the inner heliosphere, GCR particles contain ~98% nuclei and ~2% electrons and positrons, in which the nuclei consist of 87% protons, 12% helium ions and ~1% heavier ions (Simpson, 1983). On the other hand, ACRs, typically in the energy range of a few to ~100 MeV/nuc, are generally believed to be produced from interstellar neutrals that enter the heliosphere and become ionized, transported outward as pickup ions, and accelerated at the termination shock (e.g., Garcia-Munoz et al., 1973; McDonald et al., 1974). Alternatively, SEPs originate from solar eruptive events and are usually observed over a wide range of energies, from suprathermal (a few keVs) to relativistic (a few GeVs) (Reames, 2013; Desai and Giacalone, 2016). While SEPs contribute to sporadic radiation hazards and ACRs also have slight influences, radiation induced by GCRs, especially those with high-energy and high-charge ions, is the dominant source of background ionizing radiation in interplanetary space and represents a major concern for long-duration human and robotic missions beyond Earth's magnetosphere (e.g., Cucinotta et al., 2013; Norbury et al., 2019; Guo et al., 2021; Cucinotta, 2024; Dobynde and Guo, 2024).

To evaluate radiation levels, specific physical and biological quantities are employed. The absorbed dose is defined as the ratio of the deposited energy in a material to its mass and is expressed in Grays ($1 \text{ Gy} = 1 \text{ J kg}^{-1}$). Division by the accumulation time yields the absorbed dose rate (D). Advanced radiation detectors, often using coincidence techniques, measure the energy deposition distribution within a detector to produce the linear energy transfer (LET, denoted as $L \equiv dE/dx$, with the energy dE deposited along the path of dx) spectrum, which demonstrates the distribution of energy loss per unit of path length (e.g., Zeitlin et al., 2013a, 2019). According to the commonly used recommendations of the International Commission on Radiological Protection (ICRP) ICRP (1992), the radiation quality factor,

$Q = Q(L)$, is a function of LET in water (L) and serves as a biological weight to relate absorbed dose rates to dose equivalent rates (H), the latter being expressed in Sieverts ($1 \text{ Sv} = 1 \text{ J kg}^{-1}$). The averaged radiation quality factor, $\langle Q \rangle$, can then be evaluated given the energy-integrated absorbed dose and dose equivalent: $\langle Q \rangle = H/D$. It represents the overall biological effectiveness of the radiation environment, with higher values indicating a greater potential of biological damage per unit of absorbed dose.

In the heliosphere, GCR particles undergo persistent solar modulation with an 11-year cycle, during which GCR fluxes are influenced by varying solar activity, heliospheric magnetic field strength, and solar wind, resulting in reduced fluxes at solar maximum and enhanced fluxes at solar minimum (e.g., Cliver et al., 2013; Potgieter, 2013; Chowdhury et al., 2016). Consequently, the LET spectrum, which depends on the composition and energy distribution of GCRs, also varies gradually throughout the solar cycle (Looper et al., 2013; Zeitlin et al., 2016). Meanwhile, spacecraft with different structural and material configurations experience distinct shielding environments in different periods, reporting different radiation doses in their measurements. Since the overall radiation quality factor, $\langle Q \rangle$, is closely linked to the LET spectrum that varies with solar modulation and shielding thicknesses, it is essential to examine the long-term radiation environment and understand the dependence of $\langle Q \rangle$ on these factors to better assess radiation risks and design protective measures.

Over the past 20 years, multiple space missions have been launched to study the radiation environment in the inner heliosphere. These missions have collectively improved our understanding of space radiation and provided a substantial benchmark for radiation transport models (e.g., Looper et al., 2013; Matthiä et al., 2016; Matthiä and Berger, 2017; Guo et al., 2019; Simonsen et al., 2020; Zhang et al., 2022; Liu et al., 2023; Lyu et al., 2024). Among these, several radiation detectors have provided valuable measurements:

1. The Cosmic Ray Telescope for the Effects of Radiation (CRaTER, Spence et al., 2010; Mazur et al., 2011) on board the Lunar Reconnaissance Orbiter (LRO, Chin et al., 2007; Vondrak et al., 2010), launched in 2009 and orbiting the Moon, has offered invaluable data on the lunar radiation environment, including the LET spectrum and absorbed dose rate, for over 15 years (e.g., Schwadron et al., 2012; Zeitlin et al., 2013a, 2019).
2. The Lunar Lander Neutron and Dosimetry (LND, Wimmer-Schweingruber et al., 2020) experiment

on board the Chang'E-4 mission, launched in 2019, has contributed significantly to our understanding of the lunar surface radiation dose and provided insight into the radiation environment on the far side of the Moon (e.g., Zhang et al., 2020; Xu et al., 2022).

3. As a secondary payload as part of the Artemis I mission (Smith et al., 2020; Rahmanian et al., 2023), launched in 2022, the BioSentinel CubeSat (Ricco et al., 2020) has entered a permanent heliocentric orbit and transmitted physical measurements of the lunar and deep-space radiation environment in the inner heliosphere (e.g., George et al., 2024; Rahmanian et al., 2024).
4. Farther away, the Radiation Assessment Detector (RAD, Hassler et al., 2012) on the Mars Science Laboratory (MSL, Grotzinger et al., 2012) mission was launched in 2012. It has been crucial in quantifying radiation exposure on the Mars's surface and delivering critical data for future manned missions to Mars (e.g., Zeitlin et al., 2013b; Hassler et al., 2014; Ehresmann et al., 2014; Guo et al., 2021).
5. The Liulin-MO detector (Semkova et al., 2018) on board the ExoMars Trace Gas Orbiter (TGO, Vago et al., 2015) was launched in 2016. It has been orbiting Mars and measuring particle fluxes, LET spectra, and absorbed dose rates since 2018 (e.g., Semkova et al., 2021, 2023b).

In addition to the *in-situ* observations, numerous modeling studies have analyzed the deep-space radiation environment under various shielding conditions and its biological effects on human tissues. These studies are generally based on GCR models and particle transport codes (e.g., De Angelis et al., 2006; Cucinotta et al., 2010; Kim et al., 2014; Slaba et al., 2017; Banjac et al., 2018; Khaksarighiri et al., 2020; Dobynde et al., 2021; Zaman et al., 2022; Li et al., 2023; Charpentier et al., 2024). A recent study by Liu et al. (2024) provided a comprehensive analysis of several commonly-used GCR models, highlighting their strengths and limitations. Based on this study, we adopt the Badhwar-O'Neill 2020 (BON20) model (Slaba and Whitman, 2020) as the GCR model in this study, since it provides reasonably accurate proton and helium GCR fluxes in deep space. In addition, various particle transport codes have been utilized to investigate the behavior of energetic particles in deep space as well as their radiation transport and effects. Notable examples include the GEometry ANd Tracking

(GEANT4, Agostinelli et al., 2003) program, the FLUctuating KAscAd (FLUKA, Andersen et al., 2004; Battistoni et al., 2015) code, the High charge (Z) and Energy TRANspor (HZETRN, Wilson et al., 1991, 2014; Slaba et al., 2010) code, the Particle and Heavy Ion Transport code System (PHITS, Niita et al., 2006; Sato et al., 2018), and the Monte Carlo N-Particle transport code (MCNP6, Goorley et al., 2012; Kulesza et al., 2022). Many of these tools are Monte Carlo-based codes and enable detailed analyses of GCR particle interactions with different phantoms under various conditions. They provide GCR particle spectra for different shielding thicknesses and the corresponding LET spectra, allowing the derivation of $\langle Q \rangle$ values by combining the GCR models with particle transport codes.

In this work, we model the long-term LET spectrum and the corresponding $\langle Q \rangle$ values of GCRs in deep space and under shielding conditions, with the aim of quantifying variations of $\langle Q \rangle$ with solar activity and shielding thicknesses. The GCR fluxes are provided by the BON20 model with modifications considering additional contributions by ACRs when calculating the radiation dose, and GCR particle interactions with a water phantom under various shielding conditions are simulated using GEANT4. For validation, we compare our modeled results with measurements from CRaTER and TGO/Liulin-MO, as these detectors can provide long-term deep-space and/or shielded dose rates together with LET spectra. In Section 2, together with Appendix A, we describe our modeling setups and correction factors used in dose calculations, as well as instrumental details about CRaTER and TGO/Liulin-MO. Section 3 presents the modeled $\langle Q \rangle$ values for both deep space and shielding environments, followed by model–data comparisons and physical interpretations. Further discussions on elemental contributions to radiation dose, as well as on the differing $\langle Q \rangle$ variations between lighter and heavier elements over the solar cycle are provided in Section 4. Finally, our main conclusions are summarized in Section 5.

2. Methodology and Data

2.1. The BON20 Model for Deep-Space GCRs

As inputs to our radiation calculations, we adopt the GCR particle spectra provided by the BON20 model (Slaba and Whitman, 2020). BON20 numerically solves the one-dimensional Parker transport equation (Parker, 1965; Gleeson and Axford, 1967, 1968; Fisk, 1971) using a finite-difference method under the assumption of a quasi-steady, spherically symmetric heliosphere. The

model provides energy spectra for different GCR particle species modulated to 1 AU under varying solar activity conditions. In this work, we consider GCR particles ranging from hydrogen (H) to iron (Fe) nuclei, i.e., atomic number $Z = 1–26$.

In BON20, the level of solar activity is characterized by the solar modulation potential ϕ , which reflects the averaged energy loss of GCRs as they propagate from the interstellar medium into the inner heliosphere (Gleeson and Axford, 1968). The value of ϕ can be derived from the Sunspot Number (SSN) or oxygen fluxes measured by the Cosmic Ray Isotope Spectrometer (CRIS¹, Stone et al., 1998b) on board the Advanced Composition Explorer (ACE, Stone et al., 1998a) spacecraft, both serving as proxies for solar activity. While BON20 performs slightly better when driven by the ACE/CRIS data, we adopt the SSN as input owing to its long-term availability and better prediction capability. The monthly SSN data are obtained from the World Data Center SILSO², Royal Observatory of Belgium, Brussels (SILSO World Data Center, 2006–2022).

The modulation potential $\phi(t)$ is incorporated into the transport equation by varying the diffusion coefficient, thereby linking solar activity directly to the particle transport process. This approach enables BON20 to reproduce the observed GCR spectra at the heliocentric distance (r) of 1 AU with improved consistency across particle species and over different phases of the solar cycle. In subsequent calculations, the BON20-derived fluxes are treated as deep-space GCR particle fluxes, denoted as $J_Z(E)$ for different species, where E is the kinetic energy per nucleon.

Note that BON20 includes GCRs only, while ACRs in the background also contribute to the radiation environment. Currently, only a few models, such as the Cosmic-Ray Effects on MicroElectronics (CRÈME³, Tylka et al., 1997; Adams et al., 2012), incorporate both GCRs and ACRs and are publicly available. However, CRÈME provides fluxes with a yearly cadence, making it less suitable for our temporal (monthly) resolution analysis.

Instead of directly using the CRÈME fluxes in the following analysis, we use the CRÈME and BON20 comparison results to account for ACR contributions. We first refer to the long-term model comparison by Liu et al. (2024), which shows that CRÈME generally overestimates the absorbed dose rate by 2.3%, while BON20

underestimates it by 5.9% with respect to CRaTER measurements at $r = 1$ AU. Accordingly, we apply a scaling factor of $1/(1 - 0.059) \approx 1.063$ to the calculated radiation dose to account for ACR contributions at $r = 1$ AU hereafter, effectively removing the bias relative to long-term CRaTER measurements. Furthermore, since BON20 fluxes are modulated to 1 AU, radial gradients of both GCRs and ACRs must be considered for better radiation dose estimates elsewhere in the inner heliosphere, such as near Mars at $r = 1.5$ AU. The analysis and derivation of this correction factor are detailed in Appendix A, demonstrating that factors of 11.0% and 9.7% are respectively applied to the absorbed dose rate and the dose equivalent rate calculated at 1.5 AU relative to the original BON20 results.

2.2. Modeling the LET Spectrum and $\langle Q \rangle$ Factor

Calculating the average quality factor, $\langle Q \rangle$, from the modeled results requires computing both the total absorbed dose D and the total dose equivalent H in the detector. The dose equivalent is obtained for each segment of a particle track by multiplying the absorbed dose along that segment by the LET-dependent quality factor, $Q(L)$, which defined in ICRP (1992) is adopted in this work. The LET spectrum depends on the detector material, and LET in space is commonly measured in thin silicon slabs and converted to its equivalent in water. In this study, we employ a thin water spherical layer as the detector.

The transport of particles through the shielding material is simulated using the Monte Carlo radiation transport code GEANT4⁴ (Agostinelli et al., 2003). The particle–matter interactions are described by the QGSP_INCLXX_HP physics model, which combines the Quark–Gluon String Precompound (QGSP) model for particles with energies greater than 10 GeV, the Liège Intranuclear Cascade (INCLXX) model for energies below 10 GeV and the High Precision Neutron (HP) model for neutrons with energies below 20 MeV.

To compute the LET spectra in a water detector under different shielding conditions, we adopt a two-step approach. First, we calculate the radiation environment inside the aluminum shielding; then we calculate the resulting LET spectra in a thin water detector. Both steps are formulated using the response-function method (e.g., detailed in Guo et al., 2019), in which the energy range is divided into logarithmically spaced bins. Within the corresponding bin, one particle type and energy are selected randomly for each Monte Carlo run,

¹https://izw1.caltech.edu/ACE/ASC/level2/1v12DATA_CRIS.html

²<https://www.sidc.be/SILSO/datafiles>

³<https://creme.isde.vanderbilt.edu>

⁴<https://geant4.web.cern.ch/>

assuming a uniform energy distribution inside the bin. The energy bins for the primary GCRs range from $10^{0.9}$ to $10^{5.1}$ MeV with a logarithmic step of 0.1 orders of magnitude, while for secondary particles, the bins range from $10^{-9.1}$ to $10^{6.1}$ MeV with the same step size. Resulting fluxes of the LET spectrum are obtained by convolving the response functions with the bin-integrated GCR particle fluxes.

To model spacecraft shielding, we use a spherical geometry approximation which allows isotropic irradiation to be modeled using a unidirectional particle beam [Dobynde and Guo \(2021\)](#). Two configurations of the shielding setup are employed, as demonstrated in [Figure 1](#). In the first one (Method 1), we consider 16 different aluminum shells with a thickness of 0.1, 1, 5, 10, 15, 20, 25, 30, 35, 40, 50, 60, 70, 80, 90 and 100 g/cm^2 (see [Figure 1\(a\)](#)) and calculate corresponding flux-response functions inside the shielded region for each shell. The inner radius of the shell, r_{in} , is fixed at 1 m. Subsequently, the energy deposition and LET spectra are calculated in the “detector” which is approximated by a spherical water layer with an inner radius of 175 mm and a thickness of 1 mm. The LET spectrum is computed for all relevant particle species, including primary GCRs, fragmented nuclei, secondary protons, electrons, neutrons and gamma rays at the grid with energy bin edges from $10^{-9.1}$ to $10^{6.1}$ MeV with a step size of 0.1 orders of magnitude.

The second configuration (Method 2) considers only a single spherical aluminum layer with a total surface density of $100 \text{ g}/\text{cm}^2$. Flux-response functions are calculated inside the aluminum layer for 101 radial distances with a step of $1 \text{ g}/\text{cm}^2$, as illustrated in [Figure 1\(b\)](#). At each layer, inward-directed particles are considered for subsequent LET calculations (in the same manner as described above).

2.3. Measuring Absorbed Dose Rates and LET Spectra

In this study, we use data from two detectors, which operate under distinct shielding conditions, to characterize the long-term GCR radiation environment in the inner heliosphere.

Launched in June 2009 into a 50 km lunar orbit, CRaTER ([Spence et al., 2010](#); [Mazur et al., 2011](#)) on board the LRO ([Chin et al., 2007](#); [Vondrak et al., 2010](#)) carries three pairs of silicon detectors, separated by tissue-equivalent plastic (TEP) blocks. Each pair consists of a thin detector (0.15 mm for D1, D3 and D5) and a thicker detector (1.0 mm for D2, D4 and D6) with low and high amplifier gains, respectively, and providing absorbed dose rate measurements at lunar orbit. When instruments on board LRO are pointed toward the

lunar nadir, the D1 and D2 pair (hereafter “D1 and D2” denotes coincidence logic) faces deep space with minimal shielding of $0.22 \text{ g}/\text{cm}^2$, while D5 and D6 face the Moon, and D3 and D4 are positioned in the middle between two TEP blocks. Among them, the D1 and D2 pair features a wide field of view (169° out of the full angle), a large geometric factor ($24.15 \text{ cm}^2 \text{ sr}$), and a low threshold energy for incoming particles (e.g., 12.7 MeV for protons) and measures the radiation environment closest to deep-space scenario without shielding ([Spence et al., 2010](#)). Therefore, data from the D1 and D2 pair are used in our study and are publicly available in the CRaTER data center⁵. In this work, we remove transient spikes corresponding to SEP events, and the remaining absorbed dose rate primarily represents the GCR contribution. Note that the data released online are reported as absorbed dose rates in water on the lunar surface. We convert the acquired data to those in water at the Moon’s orbit, accounting for contributions from orbital altitude and secondary particles, the latter being 8.6–19.9% as reported by [Schwadron et al. \(2012\)](#) and [Zaman et al. \(2020\)](#). A detailed description of the CRaTER data conversion is presented in [Section 2.3 of Liu et al. \(2024\)](#).

In addition, we use measurements from the Liulin-MO⁶ dosimeter on board TGO ([Semkova et al., 2015, 2018](#)). Launched in March 2016 and inserted into a 400 km Mars’s orbit in April 2018 ([Vago et al., 2015](#)), TGO carries the Liulin-MO dosimetry detector, which consists of two perpendicular pairs of silicon photodiodes and corresponding amplifiers, each converting energy deposited by charged particles or photons into voltage pulses. Accounting for the shielding from the spacecraft structure and residual fuel, Liulin-MO has an aluminum-equivalent shielding ranging from ~ 1 to $100 \text{ g}/\text{cm}^2$, with an average value of $\sim 20 \text{ g}/\text{cm}^2$ ([Semkova et al., 2021](#)). The corresponding probability density function of the shielding distribution is shown in [Figure 2\(a\)](#). In our analysis, we resample the shielding thickness distribution for the 16 or 100 shielding layers described in [Section 2.2](#). We first derive the cumulative distribution profile from the original probability density function and perform resampling along that profile, as shown in [Figure 2\(b\)](#). This procedure yields a rebinned shielding thickness distribution for both methods, as shown in [Figure 2\(a\)](#). The resulting distribution is used as weighting factors for different shielding layers when constructing the modeled spectra under TGO’s shielding conditions.

⁵<https://crater-web.sr.unh.edu/>

⁶<https://esa-pro.space.bas.bg/datasources>

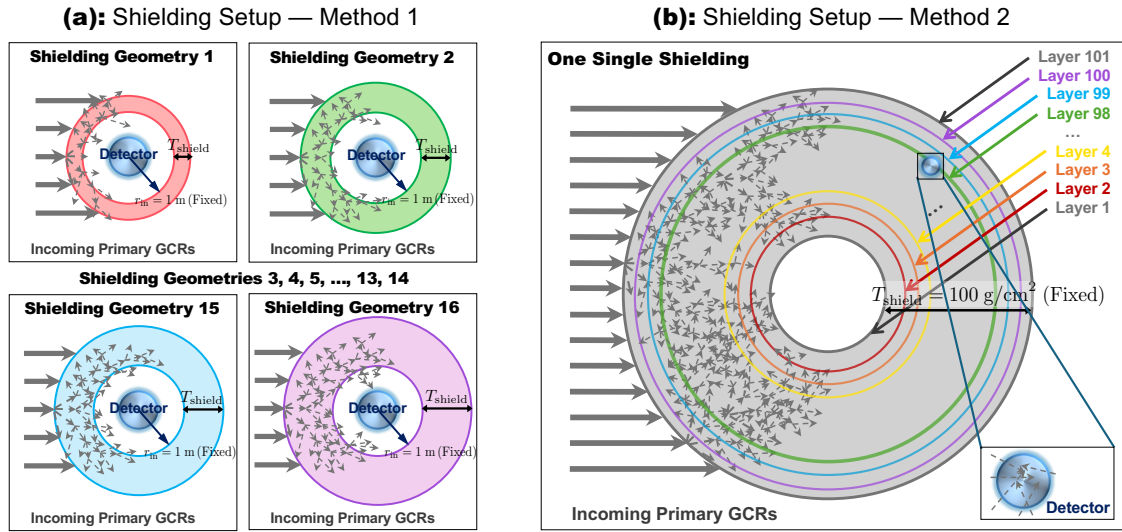


Figure 1. Schematic diagram of the shielding setup adopted in this study. The layers shown here correspond to two-dimensional plane cuts. (a) In the first method, we employ 16 distinct spherical shells, each with a specific shielding thickness (T_{shield}). The inner radius of the shielding layer (r_{in} , shown in the plot) is fixed at 1 m. (b) In the second method, we use one single spherical shell configuration with a total thickness of 100 g/cm^2 and split it into 101 concentric layers. In both approaches, isotropic primary GCRs are injected into the system. Particle fluxes inside the shielding (Method 1) or at the inner boundary of each layer (Method 2, also see a zoomed-in view at its lower-right corner) are used for dose calculations in a 1 mm thick spherical water “detector” with an inner radius of 175 mm, which is located at the center of the shielding sphere.

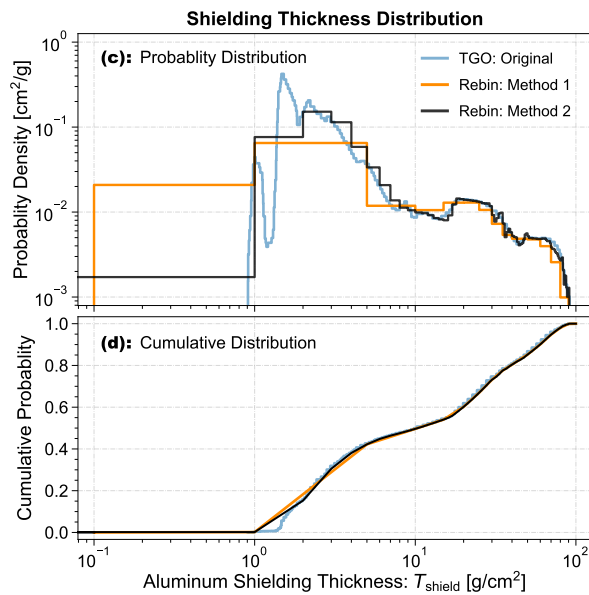


Figure 2. Shielding thickness distribution of TGO/Liulin-MO. (a) Probability distribution function. (b) Cumulative distribution function. In both panels, the original TGO/Liulin-MO shielding thickness distribution taken from Semkova et al. (2021) is shown in blue. The rebinned distribution functions corresponding to the first and second methods are shown in orange and black, respectively.

3. Results

3.1. LET Spectrum and $\langle Q \rangle$ Calculations for GCRs in Deep Space

Using the GCR spectra derived from BON20 and the response functions from GEANT4 simulations, we first present the modeled GCR spectra and corresponding LET functions in deep space for October 2019. This period, occurring near the solar minimum between Solar Cycles 24 and 25, represents a condition of low solar modulation ($\phi = 398 \text{ MV}$) and thus elevated GCR fluxes. The analysis presented in this section serves as a reference case for subsequent calculations.

Based on the monthly SSN in October 2019, we adopt a modulation potential of $\phi = 398 \text{ MV}$ for BON20 and obtain the differential energy spectra of individual GCR species, as shown in Figure 3(a). Then, Figure 3(b) presents the corresponding energy dependence of the LET in water, representing the energy loss per unit path length as GCR particles interact with the water sphere detector as illustrated in Figure 2. For each ion species, $L(E)$ rises sharply toward low energies, reflecting enhanced ionization losses near the end of the particle range (also known as the Bragg peak, Bragg and Kleeman, 1905). In fact, the magnitude of L scales approximately with Z^2/A , where A is the atomic mass, resulting in substantially higher LET values for heavier ions such as iron.

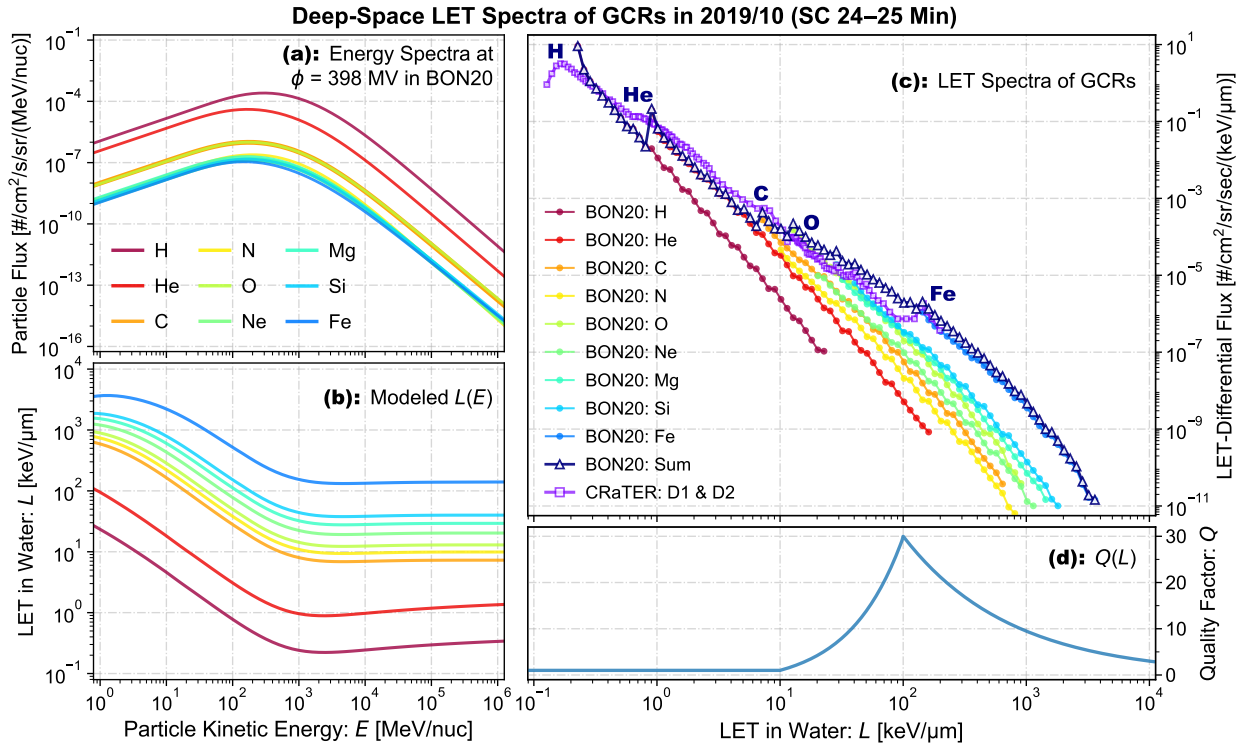


Figure 3. Deep-space GCR spectra in October 2019 (solar minimum between SCs 24 and 25) and the corresponding LET spectra. (a) GCR energy spectra of different species in BON20, with the modulation potential $\phi = 398$ MV used as the model input for this period. (b) LET distributions ($L \equiv dE/dx$) in water as functions of particle kinetic energy E for different species of GCRs. Panels (a) and (b) share the same legend shown at the bottom-left corner of panel (a). (c) Converted LET spectra of GCRs in deep space, derived from the results shown in panels (a) and (b). Curves with dotted points denote the modeled LET spectra for individual particle species; the dark-blue solid curve with triangles represents the LET spectrum summed over 26 elements (from H to Fe) in BON20, and the purple curve with squares shows measurements from the CRaTER D1 and D2 pair. Characteristic peaks in the LET spectrum for specific elements (H, He, C, O, and Fe) are marked. Detailed notations are listed at the bottom-left corner of this panel. (d) $\langle Q \rangle$ as a function of L (for LET), taken from ICRP (1992).

Combining the BON20 energy spectra and the $L(E)$ relationships, we derive the modeled LET spectra in deep space, as shown in Figure 3(c). The dotted curves correspond to individual species, while the dark-blue solid curve with triangles represents the total LET spectrum, summed over elements from H to Fe. For comparison, we also plot the GCR LET spectrum measured by the CRaTER D1–D2 detector pair (purple curve). Although data of the D1 and D2 pair correspond to a shielding thickness of 0.22 g/cm^2 , we include them here as a reference for a near-deep-space environment. Overall, the modeled total LET spectrum agrees well in both shape and magnitude with the CRaTER measurements over the range $0.3\text{--}200 \text{ keV}/\mu\text{m}$. The modeled spectrum exhibits an extended high-LET tail due to contributions from heavy nuclei such as irons, which are largely absent in measurements because of the limited coincidence statistics. At the low-LET end, the modeled spectrum shows a gradual rise followed by obvious

discontinuities at the characteristic peaks, which likely reflects distinct transitions between species and differences in the energy-loss behavior of light and heavy ions and is also found in a study by Naito and Kodaira (2022).

Finally, Figure 3(d) shows the relationship between the radiation quality factor Q and LET as recommended by the ICRP 60 report (ICRP, 1992). This function is subsequently applied to calculate the dose equivalent from the modeled LET spectra. For instance, here, by integrating the modeled LET spectrum, we obtain an absorbed dose rate of 192.7 mGy/year in water; combining with the $Q(L)$ function gives a dose equivalent rate of 1077.9 mSv/year , yielding an averaged $\langle Q \rangle$ of ~ 5.6 .

3.2. Simulations of Shielding Environments

Taking the deep-space GCR fluxes derived from BON20 as incident particle spectra, we employ two configurations as described in Section 2.2 in GEANT4

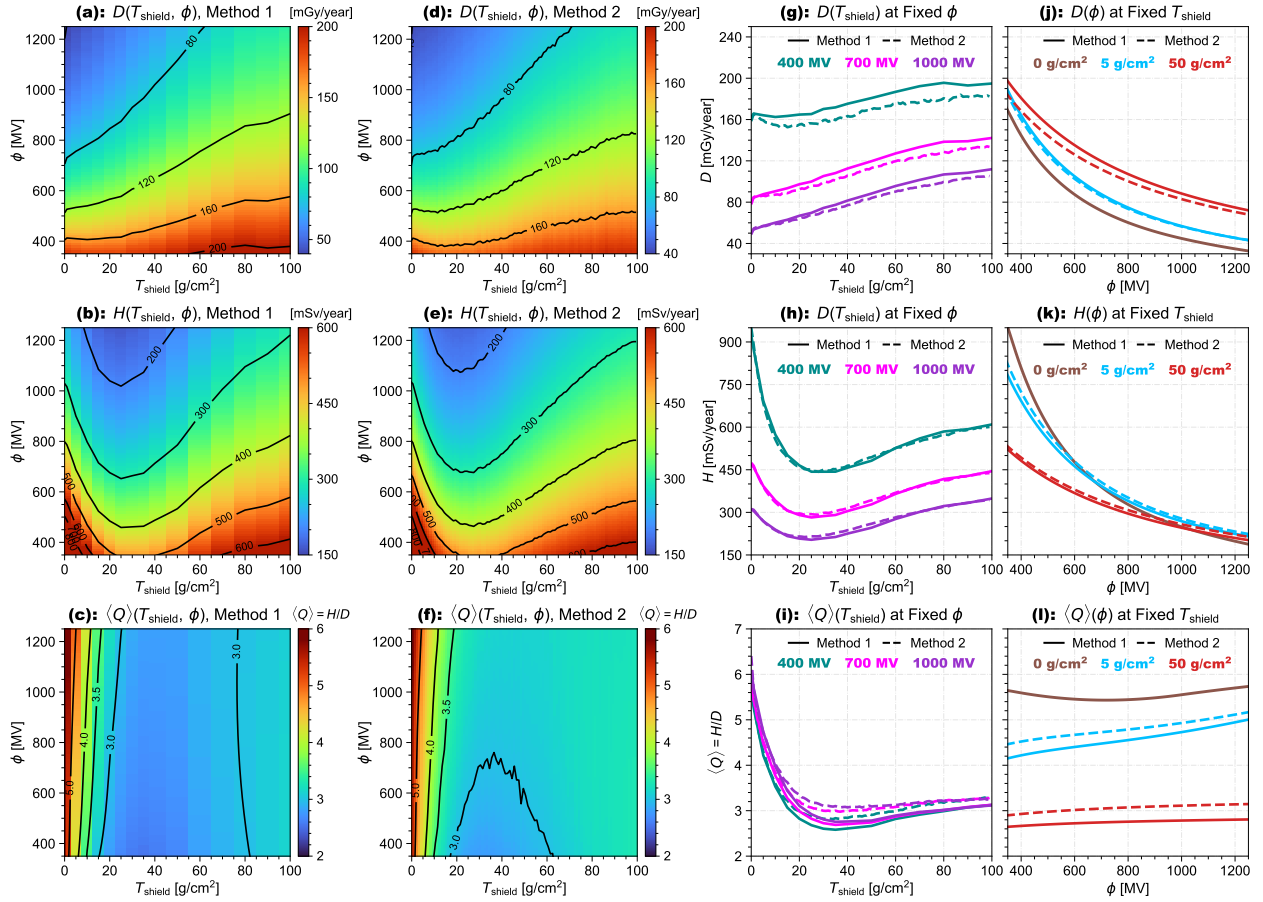


Figure 4. Absorbed dose rate (D), dose equivalent rate (H), and the radiation quality factor ($\langle Q \rangle$) under shielding conditions. (a)–(c) D , H , and $\langle Q \rangle$ obtained via the first method, shown as functions of the aluminum shielding thickness (x -axis) and solar modulation potential (y -axis). (d)–(f) Same parameters plotted in a same style as in panels (a)–(c), but obtained via the second method. (g)–(i) D , H , and $\langle Q \rangle$ as functions of the aluminum shielding thickness (x -axis) for fixed modulation potentials: $\phi = 400$ MV (green), 700 MV (magenta), and 1000 MV (purple). (j)–(l) D , H , and $\langle Q \rangle$ as functions of the solar modulation potential (x -axis) for fixed aluminum shielding thickness values: $T_{\text{shield}} = 0$ g/cm² (i.e., deep space, in brown), 5 g/cm² (blue), 50 g/cm² (red). In each panel from (g) to (l), results from the first and second methods are shown as solid lines and dashed lines, respectively.

to model the absorbed dose, dose equivalent and radiation quality factor under different aluminum shielding thicknesses. The simulations are performed for a full range of solar modulation potentials (0–2000 MV) and results for 350–1250 MV are shown to represent different phases of the solar cycle. We show the results for both simulation approaches in Figure 4 and outline the main findings below.

1. Panels (a)–(c) and (d)–(f) show values of D , H , and $\langle Q \rangle$ as functions of the aluminum shielding thickness and solar modulation potential, derived from both simulation methods, respectively. For direct comparison, the same color scale and contour style are used for the corresponding quantities in both methods. Although the model configuration setup

and the shielding thickness resolution are different, both methods exhibit consistent trends in the variation of D , H , and $\langle Q \rangle$. Notably, panels (c) and (f) reveal that $\langle Q \rangle$ depends strongly on the shielding thickness but only weakly on the modulation potential, i.e., the solar activity.

2. To highlight these variations, we plot D , H , and $\langle Q \rangle$ as functions of aluminum shielding thickness for fixed modulation potentials in panels (g)–(i), respectively. In both methods, for a given ϕ , the absorbed dose rate rises gradually with increasing shielding thicknesses, reflecting contributions from secondary particles. In contrast, the dose equivalent decreases sharply up to 10–30 g/cm² (depends on ϕ and the method), followed by a

gradual increase at larger thicknesses. In thin shielding ($<10 \text{ g/cm}^2$), H drops due to the progressive attenuation of primary GCRs, and the characteristic minima indeed arise from the competition between primary GCR attenuation and secondary particle production. In thick shielding ($>30 \text{ g/cm}^2$), H rises because of the buildup of secondary neutrons, gamma rays and light ions. Accordingly, $\langle Q \rangle$ exhibits a similar pattern, i.e., falling drastically to a minimum at $\sim 10\text{--}30 \text{ g/cm}^2$, then rising gradually toward ~ 3 at higher thicknesses. Although both methods capture these variations consistently, slight differences ($\sim 10\%$) can be found in their results, as also illustrated in panels (j)–(l). It is likely because Method 2 includes a small contribution of secondary particles generated in the inner layers that are first directed outward and inward again. Note that only inward fluxes are taken at each layer of the subsequent LET calculations.

3. Similarly, we show D , H , and $\langle Q \rangle$ as functions of the modulation potential in deep space (0 g/cm^2) and for cases with thin (5 g/cm^2) and thick (50 g/cm^2) shielding. As the modulation potential increases (i.e., from solar minimum to maximum), both D and H decrease because of the reduced GCR fluxes under stronger solar activity. The value of $\langle Q \rangle$ varies modestly with ϕ , showing a fluctuation of ~ 1 and again indicating that shielding plays a more dominant role than solar modulation in shaping the radiation quality factor.

To summarize, both simulation methods show consistent trends in D , H and $\langle Q \rangle$ as functions of aluminum shielding and solar modulation potential. The tabulated results presented above can serve as quick references for estimating the absorbed dose rate, dose equivalent rate and $\langle Q \rangle$ given specific values of shielding thickness and modulation potential. Quantitative differences in thin shielding probably originate from albedo interactions included in Method 2. As reported by Schwadron et al. (2014), $\langle Q \rangle$ reaches ~ 6 for $\phi = 400 \text{ MV}$ at a thin shielding of 1 g/cm^2 , consistent with the results obtained from both methods shown in panel (i). For the subsequent analysis, we adopt the results based on Method 1, as it provides a more realistic treatment for each given shielding thickness, while we note Method 2 may serve as a useful approximation for rapid estimates across various shielding thicknesses.

3.3. Validations against CRaTER and TGO Measurements

We next validate our modeled results by comparing them with CRaTER and TGO measurements in different shielding environments.

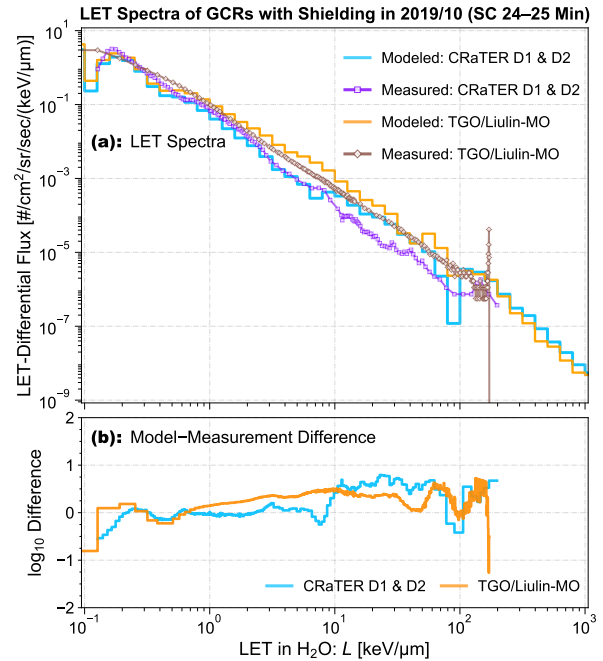


Figure 5. LET spectra of GCRs from both modeling and measurements in October 2019 (solar minimum between SCs 24 and 25). (a) Modeled and measured LET spectra. The modeled LET spectrum for the CRaTER D1 and D2 pair with a thin aluminum shielding thickness of 0.22 g/cm^2 is shown in blue, with the corresponding measured spectrum plotted as a purple curve with squares. The modeled LET spectrum for TGO/Liulin-MO, based on the shielding thickness distribution in Figure 2, is shown in orange, with the corresponding measurement plotted as a brown curve with diamonds. (b) Logarithmic differences between the modeled and measured LET spectra for CRaTER (blue) and TGO/Liulin-MO (orange).

To start with, we examine the LET spectra. As an example, in Figure 5(a), we compare the modeled and measured LET spectra for CRaTER and TGO/Liulin-MO in October 2019, corresponding to the solar minimum between SCs 24 and 25. The modeled spectrum for the CRaTER D1 and D2 pair with a thin aluminum shielding of 0.22 g/cm^2 (blue) closely reproduces the measured spectrum (purple, with squares), remaining within one order of magnitude. Similarly, the modeled LET spectrum for TGO/Liulin-MO (orange), computed using the rebinned shielding thickness distribution shown in Figure 2, overall agrees well with the measured data (brown, with diamonds). At high LET values, the measured Liulin-MO data show a notice-

able peak in the last several LET channels. This occurs because these channels include particles with LETs exceeding their nominal upper limits, leading to partial signal saturation in the instrument electronics. As a result, particles with $\text{LET} > 170 \text{ keV}/\mu\text{m}$ are redistributed among channels spanning roughly $165\text{--}177 \text{ keV}/\mu\text{m}$, with the last Liulin-MO channel corresponding to $177 \text{ keV}/\mu\text{m}$ (see also Semkova et al., 2021).

To show the quantitative difference, in Figure 5(b), we plot the logarithmic differences between the modeled and measured LET spectra for both CRaTER (blue) and TGO/Liulin-MO (orange). The modeled and measured spectra agree well at a low LET ($< 10 \text{ keV}/\mu\text{m}$), while slightly larger deviations occur at a high LET ($> 100 \text{ keV}/\mu\text{m}$), likely due to coincidence statistics and instrumental response limitations.

We then examine the temporal variations of the absorbed dose rate, dose equivalent rate, and averaged radiation quality factor, and present their evolutions alongside the SSN and ϕ values in Figure 6. Panel (a) shows the monthly SSN and the corresponding solar modulation potential adopted in the BON20 model, together illustrating the evolution of solar activity and associated modulation of GCRs. Panel (b) compares the modeled and measured absorbed dose rates D for CRaTER and TGO/Liulin-MO. For the CRaTER D1 and D2 pair, the modeled absorbed dose rate (blue) generally aligns with the measured trend (purple), and the vertical bars in the modeled curve represent uncertainties arising from lunar albedo contributions (8.6–19.9%; Schwadron et al., 2012; Zaman et al., 2020), with the central value corresponding to the median albedo contribution of 14.25%. Both the modeled and measured D values decrease during solar maximum and increase toward solar minimum, consistent with the expected GCR modulation. A generally closer match is obtained for CRaTER before 2019, while noticeable discrepancies appear afterward, likely because the BON20 calibration precedes this period and 2019–2021 appears to be at an unusually quiet solar minimum. For TGO/Liulin-MO, the modeled (orange) and measured (brown) absorbed dose rates at Mars's orbit show overall aligned temporal variations. In the modeled results, in addition to the correction factors for ACR presence and the radial gradients of GCRs and ACRs in Appendix A, albedo particle contributions are accounted for using the fractions presented in Section 3.3 of Liu et al. (2023), which vary in the range of 4–8% depending on the solar modulation at an altitude of 400 km around Mars. As the modeled albedo particle contributions in Liu et al. (2023) provide specific values, the associated uncertainties are not shown here. However, additional uncertainties may

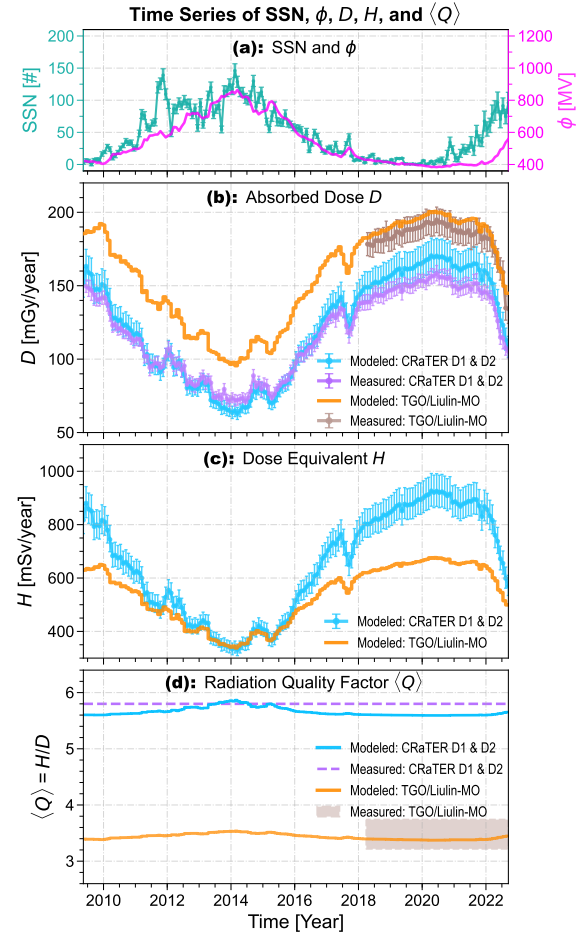


Figure 6. Time evolution of the sunspot number (SSN), solar modulation potential (ϕ) used in BON20, absorbed dose rate, dose equivalent rate, and radiation quality factor. (a) SSN (green) and ϕ (magenta), corresponding to the left and right y-axes, respectively. (b) Modeled and measured absorbed dose rates in water. The blue curve represents the modeled in-orbit absorbed dose rate for the CRaTER D1 and D2 pair, with vertical bars indicating uncertainties due to lunar albedo particle contributions. The purple curve shows measurements from the CRaTER D1 and D2 pair at the orbit of the Moon, plotted in a monthly cadence, with vertical bars for the standard variation of daily measurements within each month. The orange and brown curves indicate the modeled and measured TGO/Liulin-MO absorbed dose rate at Mars's orbit, with brown vertical bars denoting the standard variations of measurements. (c) Modeled in-orbit dose equivalent rates in water for the CRaTER D1 and D2 pair (blue) and TGO/Liulin-MO (orange). The vertical bars for the CRaTER D1 and D2 pair accounts for uncertainties due to varying lunar albedo particle contributions. The Martian albedo contribution is also included in the model, but the uncertainty is not shown (see more explanations in the text). (d) Radiation quality factor (Q). The blue curve represents our modeled (Q) corresponding to the environment where the CRaTER D1 and D2 pair is exposed to, while the dashed purple curve shows the value derived from the CRaTER D1 and D2 pair measurements (5.8, from Zeitlin et al., 2013a). The orange curve represents our modeled (Q) for the TGO/Liulin-MO environment, and the brown shaded region shows the corresponding measurements (3.49 ± 0.26 , from Semkova et al., 2021).

arise from the variability of the model inputs (e.g., SSN) and from the regolith composition and physical properties of the Martian surface (e.g., Röstel et al., 2020), which influence the generation and transport of albedo particles and is beyond the scope of this study. The measured data are converted to dose rates in water with a factor of 1.333, as derived in Appendix B of Schwadron et al. (2012). Both modeled and measured values for TGO/Liulin-MO are systematically higher than those for CRaTER, due to (1) enhanced contributions from secondary particles under the thicker shielding environment (see also, e.g., Dobynde et al., 2019; Xu et al., 2022; Zhang et al., 2022; Liu et al., 2023), and (2) radial gradient of the GCR and ACR fluxes between Earth and Mars, as detailed in Appendix A.

We plot the modeled dose equivalent rates H in panel (c), which exhibit similar temporal variations as the absorbed dose rate. While the absorbed dose rate for TGO/Liulin-MO is systematically higher than that for CRaTER, the corresponding dose equivalent rate is lower, particularly near solar minimum, with a reduction of about 30%. This consistent decrease reflects the shielding effects that preferentially attenuate high-LET components contributing more strongly to the dose equivalent.

In panel (d), we compare the modeled and measured $\langle Q \rangle$ values for GCRs under CRaTER and TGO shielding conditions. Note that the acquired measured LET spectra (Figures 3(c) and 5(a)) cover a limited LET range due to coincidence statistics. Hence, they are used only for comparison with the modeled LET spectrum, while literature values of $\langle Q \rangle$ derived by the instrument teams are adopted for the following quantitative comparisons. As shown, our modeled $\langle Q \rangle$ for the CRaTER D1 and D2 pair (blue) closely matches the measurement-derived value of 5.8 (Zeitlin et al., 2013a). Besides, our modeled $\langle Q \rangle$ for TGO/Liulin-MO (orange), which includes the contribution by neutrons and gamma rays based on Mitrofanov et al. (2018) and Semkova et al. (2023a), agrees well with the measured 3.49 ± 0.26 (Semkova et al., 2021). We also find a modest variation of $\langle Q \rangle$ during SC 24 maximum in our modeled results, which is up to 0.4 for the CRaTER D1 and D2 pair and up to 0.2 for TGO/Liulin-MO, indicating that $\langle Q \rangle$ is relatively insensitive to solar modulation. This trend in both CRaTER and TGO further confirms that shielding properties play a more dominant role than heliospheric modulation in determining the radiation quality factor for GCRs, consistent with a recent study by Naito and Kodaira (2025).

4. Discussion

While the GCR fluxes vary with the solar modulation, the resulting $\langle Q \rangle$ exhibits only a weak dependence on it. To understand why $\langle Q \rangle$ is relatively insensitive to solar activity, we next investigate and discuss the contributions from individual GCR elements from a modeling perspective.

4.1. Radiation Dose Contribution from Individual GCR Elements

To quantify the elemental contributions to the overall radiation environment, we decompose the absorbed dose rate, dose equivalent rate, and radiation quality factor into contributions from individual GCR elements from hydrogen to iron, denoted as D_Z , H_Z and $\langle Q \rangle_Z$, respectively.

Figure 7 shows these elemental quantities of deep-space GCRs derived from BON20 for two representative periods: February 2014 (SC 24 maximum) and October 2019 (SC 24–25 minimum). In the figure, D_Z and H_Z are plotted as vertical bars corresponding to the left y-axis on a logarithmic scale, while $\langle Q \rangle_Z$ values are shown as scatter points overlaid on the respective bars and aligned to the right y-axis. Also, we use black arrows to connect the $\langle Q \rangle_Z$ values between the two periods, illustrating their variation with respect to solar activity for each element. We list our main findings and provide explanations in the following.

1. Elemental dominance in dose and dose equivalent: Consistent with the findings in Section 3.2 of Liu et al. (2024), H and He dominate the absorbed dose during both solar maximum and minimum. However, they do not dominate the dose equivalent. Instead, several heavier ions, such as carbon (C), oxygen (O), magnesium (Mg), silicon (Si), calcium (Ca), titanium (Ti), chromium (Cr) and Fe, make relatively small contributions to the absorbed dose but large contributions to the dose equivalent. This contrast arises from their higher LET values, as shown in Figure 3(c).
2. Atomic number dependence of $\langle Q \rangle_Z$: The elemental radiation quality factor generally increases with atomic number for both periods, reflecting the higher LET of heavier nuclei due to their larger charge and mass. The $\langle Q \rangle_Z$ value rises from ~ 1 to ~ 25 for species from H to scandium (Sc), and then gradually decreases for heavier species ($Z > 21$). This decline for heavier nuclei occurs because their

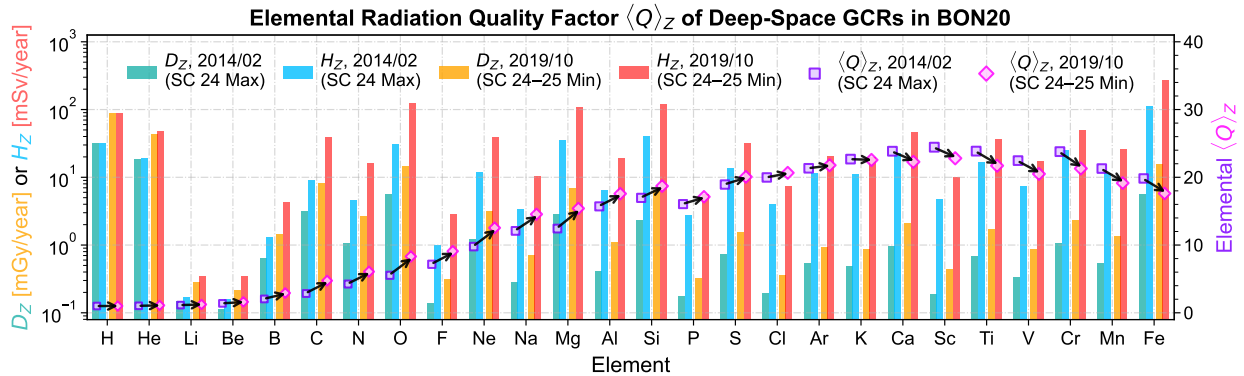


Figure 7. Elemental absorbed dose rate (D_Z), dose equivalent rate (H_Z), and radiation quality factor ($\langle Q \rangle_Z$) of deep-space GCRs derived from the BON20 model. D_Z and H_Z correspond to the left y-axis (logarithmic scale), while $\langle Q \rangle_Z$ corresponds to the right y-axis. For each element from H to Fe, absorbed dose and dose equivalent rates are shown as green and blue vertical bars for February 2014 (SC 24 maximum), and as orange and red vertical bars for October 2019 (SC 24–25 minimum), respectively. The corresponding $\langle Q \rangle_Z$ in these two periods are plotted as purple squares and pink diamonds, respectively, with marker sizes scaled according to their values. Black arrows connect the calculated $\langle Q \rangle_Z$ scatter points during these two periods for each element to better illustrate the variation of $\langle Q \rangle_Z$ with solar activity.

LET falls beyond ~ 100 keV/ μm , where the quality factor $Q(L)$ begins to fall, as shown in Figure 3(c)(d).

3. Solar activity dependence of $\langle Q \rangle_Z$ across elements: In addition to the atomic number dependence, we find a distinct trend in how $\langle Q \rangle_Z$ changes from solar maximum to minimum. For lighter elements, $\langle Q \rangle_Z$ increases with reduced solar activity, whereas it decreases for heavier elements starting from Ca, i.e., $Z \geq 20$. This contrasting behavior actually reflects differences in the radiation impact caused by GCR modulation and the energy dependence of LET among light and heavy ions, which we further discuss in the next section.

In summary, the modulation of $\langle Q \rangle_Z$ with solar activity depends strongly on elemental mass and charge. In order to elucidate the underlying physics of the contrasting behavior mentioned above, we analyze how $\langle Q \rangle_Z$ evolves with solar modulation for light and heavy species in the following.

4.2. $\langle Q \rangle_Z$ of Lighter and Heavier GCR Elements During Solar Minimum and Maximum

To start with, we examine the He and Fe particle fluxes, representative of light and heavy species, respectively. Figure 8 shows the modeled He and Fe fluxes in deep space during February 2014 (SC 24 maximum) and October 2019 (SC 24–25 minimum) with corresponding measurements from the Alpha Magnetic Spectrometer (AMS-02, Aguilar et al., 2022) and ACE/CRIS, respectively. Panels (a) and (d) show the

absolute particle fluxes (J_Z), and panels (b) and (e) show the flux ratios between solar minimum and maximum. The measurements are overlaid in these four panels, demonstrating good agreement with the BON20 model predictions in GCR particle fluxes. Taking the energy-dependent LET functions and the corresponding $Q(L)$ in Figures 3(b)(d), panels (c) and (f) relate the particle kinetic energy, E , to LET, $L(E)$, and further the radiation quality factor $Q(L(E))$.

By comparing the GCR fluxes for He and Fe during solar maximum and minimum, we can see how the GCR spectra and the energy-dependent LET function jointly determine the elemental contribution to $\langle Q \rangle_Z$. During solar maximum, low-energy GCR particles are strongly modulated, leading to a substantial reduction in their fluxes. In contrast, during solar minimum, the relative importance of low-energy ions is enhanced, leading to higher $\langle Q \rangle_Z$ for lighter elements, whose LET rises sharply at lower energies. However, for heavier elements such as Fe, the relative importance of higher-energy component within the spectra, which corresponds to a higher Q , is reduced during solar minimum. Thus, $\langle Q \rangle_Z$ is smaller during solar minimum than solar maximum. This above analysis of particle fluxes and their energy-dependent LET explains the contrasting response of $\langle Q \rangle_Z$ for light and heavy elements to solar modulation, as shown in Figure 7.

Furthermore, we investigate the temporal and ϕ -dependent variations of D_Z , H_Z and $\langle Q \rangle_Z$ for selected GCR elements (H, He, C, O, Mg, Si, Ca, Ti, Cr and Fe) in deep space. These elements are chosen to represent a broad range of atomic numbers and to highlight the dif-

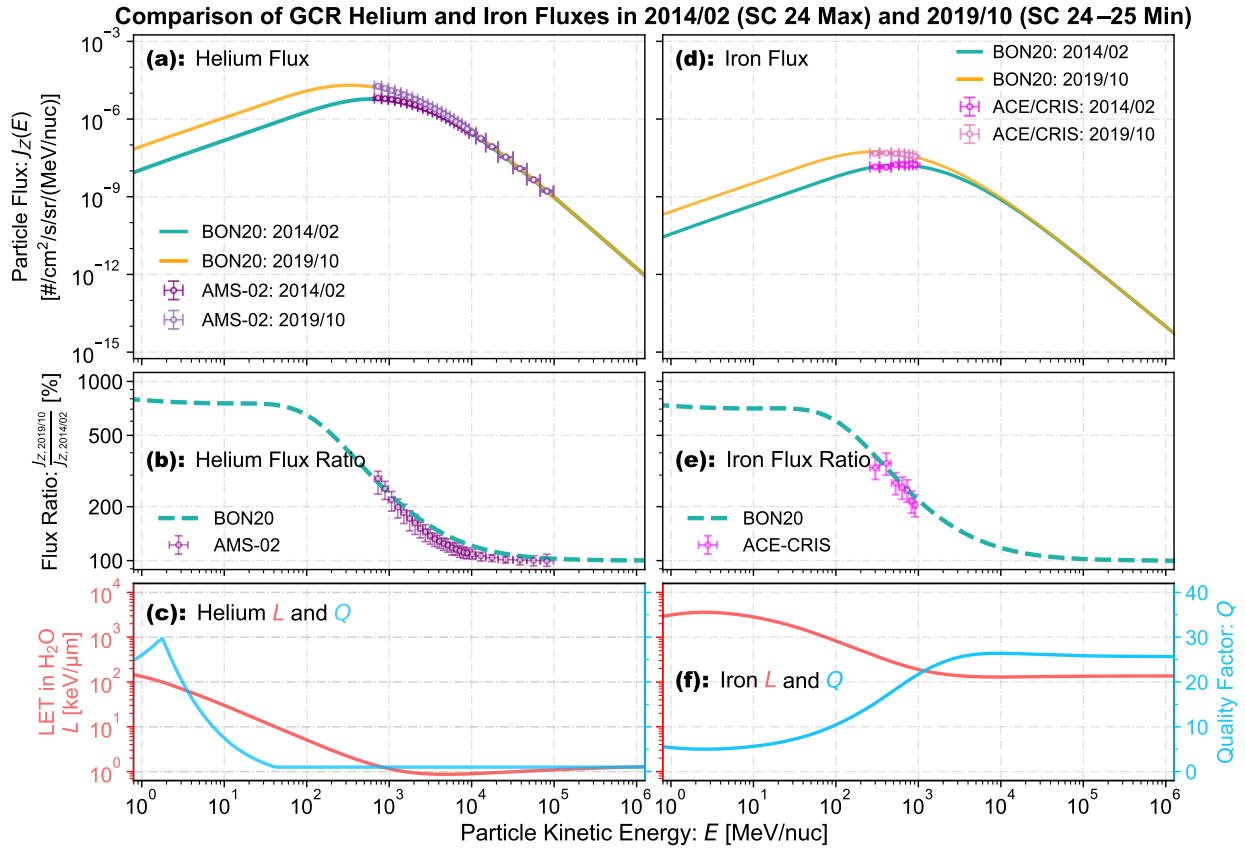


Figure 8. Comparison of particle fluxes in February 2014 (SC 24 maximum) and October 2019 (SC 24–25 minimum) for deep-space GCR helium and iron nuclei. (a) Helium fluxes. The green and orange curves represent the modeled helium particle fluxes in February 2014 and October 2019, respectively, with the light- and dark-purple scatter points indicating AMS-02 measurements during the corresponding periods. Horizontal and vertical bars on the AMS-02 points indicate the energy bin width and systematic uncertainties of the measurements, respectively. (b) Ratio of helium fluxes in October 2019 to those in February 2014. The green line shows the BON20 results, and the purple scatter points show AMS-02 measurements, with horizontal and vertical bars for the energy bin width and systematic uncertainties, respectively. (c) The helium LET function (red, left y-axis) and the radiation quality factor Q (blue, right y-axis) as functions of the particle kinetic energy, converted based on Figure 3(a)(b)(d). (d)–(f) Iron fluxes, the flux ratio, LET function and Q plotted as functions of the particle kinetic energy, following the same pattern as panels (a)–(c), except using ACE/CRIS measurements shown in light-pink and/or magenta.

fering contributions of light and heavy ions to D_Z , H_Z and $\langle Q \rangle_Z$ illustrated in Figure 7.

Figure 9 shows these quantities in terms of their proportional contributions in different rows, from 1964 to 2022 (left column), and for ϕ values ranging from 350 to 1250 MV (right column). Alternating gray and white backgrounds in the left-column panels indicate different solar cycles, with purple and pink arrows marking solar minima and maxima, respectively, indicating how each element responds to long-term solar modulation. In panels (a) and (b), the proportionality of D_Z exhibits little variation over time or ϕ for each selected element, reflecting similar modulation effects on the absorbed dose across GCR species. On the contrary, the proportionality of H_Z shows clear element-dependent trends.

As shown in panels (c) and (d), H and He remain nearly constant, whereas Ca, Ti, Cr and Fe increase with ϕ , each varying between 3–10%, while C, O, Mg and Si decrease, each varying in the range of 1–12%. Consequently, $\langle Q \rangle_Z$ increases with ϕ for Ca, Ti, Cr, and Fe, decreases for C, O, Mg, and Si, and remains nearly constant for H and He, which is mainly governed by the energy dependence of their LET and the corresponding $Q(L)$. Taken together, the overall radiation quality factor $\langle Q \rangle$ results from a balance between these opposing trends among different GCR species, making it relatively insensitive to solar modulation.

It is important to note that the above results are based on GCR fluxes in deep space, whereas shielding would modify the GCR spectra with heavy ions fragmented

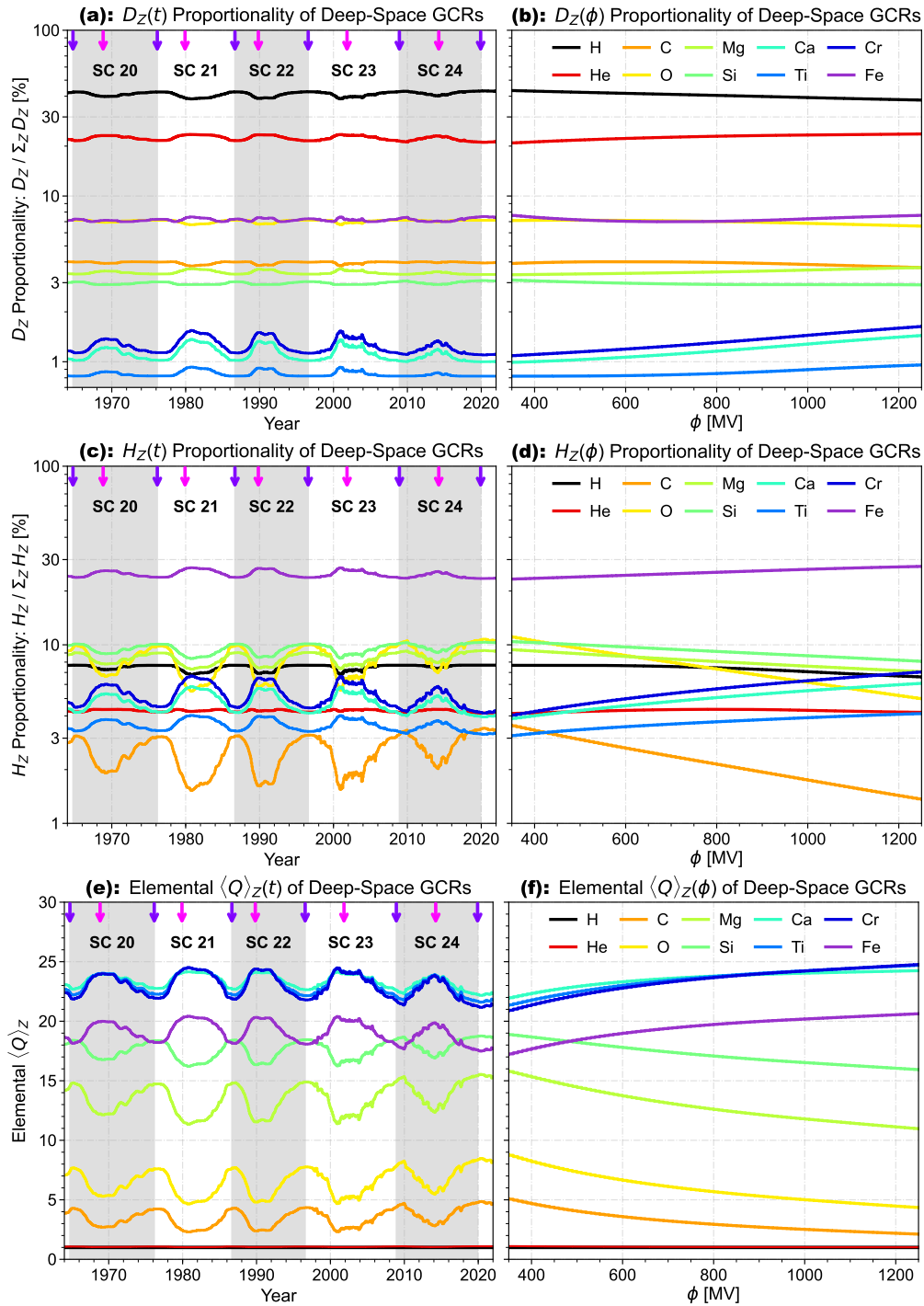


Figure 9. The absorbed dose rate proportionality, dose equivalent rate proportionality, and radiation quality factor for 10 selective elements of deep-space GCRs in BON20. (a) Absorbed dose rate proportionalities (on a logarithmic scale for better visualization) as functions of time between 1964 and 2022 for each selected element. Alternating gray and white backgrounds indicate different solar cycles, with purple and magenta arrows at the top marking solar minima and maxima, respectively. (b) Absorbed dose rate proportionalities as functions of ϕ for the same elements as shown in panel (a). Panels (a) and (b) share the same y-axis and legend, with the latter listed at the top of panel (b). (c, d) Dose equivalent rate proportionalities (on a logarithmic scale, for better visualization) for each selected element, presented in the same layout as in panels (a)(b). (e, f) Elemental radiation quality factor shown following the same layout as in panels (a)(b).

easily into lighter ones. With shielding, the contribution of heavy ions to both absorbed dose and dose equivalent would decrease significantly. In addition, secondary particles such as neutrons generated within the shielding would make additional contributions.

5. Summary and Conclusions

Understanding the long-term modulation of GCRs and their resulting radiobiological effects is essential for evaluating space radiation hazards in deep space and planetary environments. In this study, we systematically model the temporal and modulation potential variations of the LET spectra, absorbed dose rate, dose equivalent rate and radiation quality factor of GCRs in both deep space and shielding environments.

Using the SSN as input, the BON20 model is adopted to provide primary GCR spectra under different solar modulation potentials. These spectra are then used as primary particles for simulations of GCR interactions with shielding layers of different thicknesses to derive LET spectra, D , H and $\langle Q \rangle$. The results provide a comprehensive dataset spanning a broad range of solar modulations and shielding conditions, making it convenient to quickly estimate the D , H and $\langle Q \rangle$ of GCRs given ϕ and shielding thickness. In the modeled results, we find that $\langle Q \rangle$ depends strongly on shielding thickness but only weakly on solar activity. We then validate the model predictions against long-term measurements from the CRaTER D1 and D2 pair facing deep space at the Moon's orbit and the TGO/Liulin-MO instrument at Mars's orbit. In this comparison, we account for factors including the phantom medium where radiation dose is deposited (water/silicon), orbital altitude of the spacecraft, albedo particle contributions, ACR contributions and the radial gradients of both GCRs and ACRs. With these factors taken into account, our modeled absorbed dose and $\langle Q \rangle$ show consistent temporal variations with the CRaTER and TGO measurements under thin and thick shielding conditions, respectively.

To interpret the insensitivity of $\langle Q \rangle$ to solar activity, we further analyze the elemental contributions of D_Z , H_Z , and $\langle Q \rangle_Z$ across GCR species. Lighter elements, such as H and He, dominate the absorbed dose but contribute less to dose equivalent, whereas heavier ions, including C, O, Mg, Si, Ca, Ti, Cr and Fe, have greater influence on dose equivalent and thus $\langle Q \rangle$ because of their higher LET. Solar modulation primarily affects low-energy particles, thereby altering the relative weighting of particle fluxes across energies. This leads to opposite responses of $\langle Q \rangle$ for light and heavy nuclei due to their differing energy-dependent quality factors at

low energies. Consequently, the overall $\langle Q \rangle$ represents a balance between these contrasting tendencies of H_Z and $\langle Q \rangle_Z$ among different GCR species. Here, our analysis provides a physical basis for element-specific radiobiological variation in response to solar modulation and explains the weak dependence of the overall radiation quality factor $\langle Q \rangle$ on solar activity.

Acknowledgments

The authors acknowledge the support by the National Natural Science Foundation of China (Grant Nos. 42521007, 42188101 and 42474221). The authors also express their gratitude to the groups developing the BON20 GCR model and the GEANT4 toolkit, the World Data Center SILSO, Royal Observatory of Belgium, Brussels, and the teams of ACE/CRIS, AMS-02, LRO/CRaTER and TGO/Liulin-MO instruments for providing valuable data involved in this study.

Appendix A. Calculations of ACR Contributions, and GCR and ACR Radial Gradients

To account for ACR contributions and the radial gradients of GCRs and ACRs, we first consider the long-term average absorbed dose rate at 1 AU over the period 2009–2022. As stated in Section 2.1, correction factors of +2.3% for CRÈME and –5.9% for BON20 (Liu et al., 2024) are applied to remove systematic biases in the modeled absorbed dose rates compared with CRaTER measurements at 1 AU:

$$D_{\text{GCR}}(r = 1 \text{ AU}, t) + D_{\text{ACR}}(r = 1 \text{ AU}, t) \quad (\text{A.1})$$

$$= D_{\text{CRÈME}}^*(t) \equiv \frac{D_{\text{CRÈME}}(t)}{1 + 0.023} = \sum_{Z=1}^{26} D_{Z, \text{CRÈME}}(t) \quad (\text{A.2})$$

$$= D_{\text{BON20}}^*(t) \equiv \frac{D_{\text{BON20}}(t)}{1 - 0.059} = \sum_{Z=1}^{26} D_{Z, \text{BON20}}(t), \quad (\text{A.3})$$

where $D_{\text{GCR}}(r = 1 \text{ AU}, t)$ and $D_{\text{ACR}}(r = 1 \text{ AU}, t)$ denote absorbed dose rates caused by GCRs and ACRs at 1 AU, respectively, given a specific time t . $D_{\text{CRÈME}}^*(t)$ and $D_{\text{BON20}}^*(t)$ are the bias-corrected modeled dose rates summed over all species Z .

Note that BON20 only incorporates GCRs, whereas $D_{\text{BON20}}^*(t)$ in Equation (A.3) includes both ACR and GCR contributed dose:

$$D_{\text{BON20}}(t) = D_{\text{GCR}}(r = 1 \text{ AU}, t), \quad (\text{A.4})$$

$$\Rightarrow \left\langle \frac{D_{\text{ACR}}(r = 1 \text{ AU}, t)}{D_{\text{GCR}}(r = 1 \text{ AU}, t)} \right\rangle_t = \left\langle \frac{D_{\text{BON20}}^*}{D_{\text{BON20}}} \right\rangle_t - 1 = 6.3\%, \quad (\text{A.5})$$

in which $\langle \dots \rangle_t$ denotes the long-term average of the given functions. Hence, Equation (A.3) is interpreted as including the ACR contribution at 1 AU, which amounts on average to 6.3% of the calculated GCR dose.

Since BON20 fluxes are modulated to 1 AU, the radial gradients of both GCRs and ACRs should be considered for an accurate estimate of radiation doses at other heliocentric distances. For GCRs, observations indicate a radial gradient ($G_{r,\text{GCR}}$) of 2–4%/AU in the inner heliosphere (e.g., Gieseler and Heber, 2016; Vos and Potgieter, 2016; Honig et al., 2019; Roussos et al., 2020). Therefore, we adopt a representative value of 3.0%/AU in our calculations. The absorbed dose for GCRs of species Z at r is expressed as (omitting t shortly for notational simplicity):

$$D_{Z,\text{GCR}}(r) \simeq D_{Z,\text{GCR}}(r = 1 \text{ AU}) + D'_{Z,\text{GCR}}(r) \cdot \Delta r \quad (\text{A.6})$$

$$= D_{Z,\text{GCR}}(r = 1 \text{ AU}) \cdot \left[1 + \frac{D'_{Z,\text{GCR}}(r)}{D_{Z,\text{GCR}}(r = 1 \text{ AU})} \Delta r \right] \quad (\text{A.7})$$

$$\simeq D_{Z,\text{GCR}}(r = 1 \text{ AU}) \cdot \left[1 + \frac{J'_{Z,\text{GCR}}(r)}{J_{Z,\text{GCR}}(r = 1 \text{ AU})} \Delta r \right] \quad (\text{A.8})$$

$$\simeq D_{Z,\text{GCR}}(r = 1 \text{ AU}) \cdot (1 + G_{r,Z,\text{GCR}} \cdot \Delta r), \quad (\text{A.9})$$

in which $\Delta r = r - 1 \text{ AU}$.

While spectra of H, He, C, nitrogen (N), O, neon (Ne), and argon (Ar) have been identified with ACR components at low energies during solar minimum (e.g., Cummings and Stone, 1996; Marquardt et al., 2018; Giacalone et al., 2022), we primarily focus on He, N and O in this work, because H and C exhibit small model-to-model variations (Liu et al., 2024), and Ne and Ar contribute negligibly to the dose and lack reliable gradient constraints. For ACRs, observations show a radial gradient ($G_{r,Z,\text{ACR}}$) of $\sim 25\%$ /AU for He within 0.94 AU (Rankin et al., 2021) and $(49.4 \pm 8.0)\%$ /AU for O over 0.1–0.94 AU during the SC 24–25 minimum (Rankin et al., 2022). Although our study extends slightly beyond this radial range ($r = 1.5 \text{ AU}$), these values are adopted as they are representative of the period when TGO has been at Mars's orbit (since 2018), and the corresponding gradients remain relatively similar over both distance and time (see Rankin et al., 2021, 2022, and references therein). For N, we adopt the same gradient as O due to their comparable mass and charge. Similar to Equations (A.6)–(A.8), the absorbed dose for ACRs

of species Z at (r, t) is:

$$D_{Z,\text{ACR}}(r, t) \simeq D_{Z,\text{ACR}}(r = 1 \text{ AU}, t) \cdot (1 + G_{r,Z,\text{ACR}} \cdot \Delta r), \quad (\text{A.10})$$

where $D_{Z,\text{ACR}}(r = 1 \text{ AU}, t)$, with $Z = 2, 7$ and 8 , can be estimated by combining Equations (A.1)–(A.4):

$$D_{Z,\text{ACR}}(r = 1 \text{ AU}, t) \simeq D_{Z,\text{GCR}}(r = 1 \text{ AU}, t) \cdot \left\langle \frac{D_{Z,\text{ACR}}(r = 1 \text{ AU}, t)}{D_{Z,\text{GCR}}(r = 1 \text{ AU}, t)} \right\rangle_t \quad (\text{A.11})$$

$$= D_{Z,\text{BON20}}(t) \cdot \left\langle \frac{D_{Z,\text{CRÈME}}^*(t)}{D_{Z,\text{BON20}}(t)} \right\rangle_t. \quad (\text{A.12})$$

Table A.1 summarizes the parameters used for dose corrections. Applying Equations (A.9), (A.10) and (A.12) yields the total absorbed dose by GCRs and ACRs:

$$D_{\text{GCR}}(r, t) + D_{\text{ACR}}(r, t) = D_{\text{BON20}}(t) \cdot (1 + G_{r,\text{GCR}} \cdot \Delta r) + \sum_{Z=2,7,8} D_{Z,\text{BON20}}(t) \cdot \left\langle \frac{D_{Z,\text{CRÈME}}^*(t)}{D_{Z,\text{BON20}}(t)} \right\rangle_t \cdot (1 + G_{r,Z,\text{ACR}} \cdot \Delta r), \quad (\text{A.13})$$

and the dose equivalent H is corrected in the same manner. For convenience, we compute the time-averaged correction factors for the GCR and ACR contributions in Equation (A.13) and apply these averaged factors to absorbed dose and dose equivalent estimates in deep space or under different shielding conditions:

$$C_{r,\text{GCR+ACR}} = \left\langle \frac{D_{\text{GCR}}(r, t)}{D_{\text{GCR}}(r = 1 \text{ AU}, t)} \right\rangle_t + \left\langle \frac{D_{\text{ACR}}(r, t)}{D_{\text{ACR}}(r = 1 \text{ AU}, t)} \right\rangle_t. \quad (\text{A.14})$$

At $r = 1.5 \text{ AU}$ ($\Delta r = 0.5 \text{ AU}$), the correction yields a 1.75% increase in both D and H due to GCR gradients, and $(9.5 \pm 0.06)\%$ and $(8.2 \pm 1.3)\%$ increases in D and H , respectively, due to ACR contributions. Interestingly, at 1 AU, Equation (A.14) gives $(5.2 \pm 0.06)\%$ and $(5.7 \pm 0.7)\%$ increases in D and H , respectively, consistent with the 6.3% estimate from Equation (A.5), confirming that including only He, N, and O provides a reasonable approximation of total ACR effects. Therefore, we adopt correction factors of 11.0% for D and 9.7% for H for long-term deep-space and shielded dose rates at Mars, although some deviations may occur for different shielding thicknesses.

References

Adams, J., Barghouty, A.F., Mendenhall, M., Reed, R., Sierawski, B., Warren, K., Watts, J., Weller, R., 2012. CRÈME: The 2011

Table A.1. Parameters used to calculate the absorbed dose and dose equivalent rates in the inner heliosphere of Equation (A.13), accounting for the radial gradient of GCRs and ACRs in this work.

Particles	G_r [%/AU]	$\left\langle \frac{D_{Z,CRÈME}^*(t)}{D_{Z,BON20}^*(t)} \right\rangle_t$	$\left\langle \frac{H_{Z,CRÈME}^*(t)}{H_{Z,BON20}^*(t)} \right\rangle_t$
GCRs (All)	3.0	–	–
ACR/He	25.0	1.061	1.288
ACR/O	49.4	1.344	2.245
ACR/N	49.4	1.552	2.419

revision of the cosmic ray effects on micro-electronics code. IEEE Transactions on Nuclear Science 59, 3141–3147. doi:10.1109/TNS.2012.2218831.

Agostinelli, S., Allison, J., Amako, K., Apostolakis, J., Araujo, H., Arce, P., Asai, M., Axen, D., Banerjee, S., Barrand, G., et al., 2003. GEANT4: a simulation toolkit. Nuclear Instruments and Methods in Physics Research Section A 506, 250–303. doi:10.1016/S0168-9002(03)01368-8.

Aguilar, M., Cavazonza, L.A., Ambrosi, G., Arruda, L., Attig, N., Barao, F., Barrin, L., Bartoloni, A., Başeğmez-du Pree, S., Battiston, R., et al., 2022. Properties of daily helium fluxes. Physical review letters 128, 231102. doi:10.1103/PhysRevLett.128.231102.

Andersen, V., Ballarini, F., Battistoni, G., Campanella, M., Carboni, M., Cerutti, F., Empl, A., Fasso, A., Ferrari, A., Gadioli, E., et al., 2004. The FLUKA code for space applications: recent developments. Advances in Space Research 34, 1302–1310. doi:10.1016/j.asr.2003.03.045.

Banjac, S., Herbst, K., Heber, B., 2018. The atmospheric radiation interaction simulator (ATrIS) - description and validation. Journal of Geophysical Research: Space Physics 123. doi:10.1029/2018JA026042.

Battistoni, G., Boehlen, T., Cerutti, F., Chin, P.W., Esposito, L.S., Fasso, A., Ferrari, A., Lechner, A., Empl, A., Mairani, A., et al., 2015. Overview of the FLUKA code. Annals of Nuclear Energy 82, 10–18. doi:10.1016/j.anucene.2014.11.007.

Bragg, W.H., Kleeman, R., 1905. Xxxx. on the α particles of radium, and their loss of range in passing through various atoms and molecules. The London, Edinburgh, and Dublin Philosophical Magazine and Journal of Science 10, 318–340. URL: 10.1080/14786440509463378.

Charpentier, G., Ruffenach, M., Benacquista, R., Ecoffet, R., Cappe, A., Dossat, C., Varotsou, A., Cintas, H., Paillet, A., Boyer, L., et al., 2024. ARAMIS: a Martian radiative environment model built from GEANT4 simulations. Journal of Space Weather and Space Climate 14. doi:10.1051/swsc/2024032.

Chin, G., Brylow, S., Foote, M., Garvin, J., Kasper, J., Keller, J., Litvak, M., Mitrofanov, I., Paige, D., Raney, K., et al., 2007. Lunar reconnaissance orbiter overview: The instrument suite and mission. Space Science Reviews 129, 391–419. doi:10.1007/s11214-007-9153-y.

Chowdhury, P., Kudela, K., Moon, Y.J., 2016. A study of heliospheric modulation and periodicities of galactic cosmic rays during cycle 24. Solar Physics 291, 581–602. doi:10.1007/s11207-016-0945-7.

Clover, E., Richardson, I., Ling, A., 2013. Solar drivers of 11-yr and long-term cosmic ray modulation. Space Science Reviews 176, 3–19. doi:10.1007/s11214-011-9746-3.

Cucinotta, F.A., 2024. Non-targeted effects and space radiation

risks for astronauts on multiple international space station and lunar missions. Life Sciences in Space Research 40, 166–175. doi:10.1016/j.lssr.2023.08.003.

Cucinotta, F.A., Hu, S., Schwadron, N.A., Kozarev, K., Townsend, L.W., Kim, M.H.Y., 2010. Space radiation risk limits and earth-moon-mars environmental models. Space Weather 8. doi:10.1029/2010SW000572.

Cucinotta, F.A., Kim, M.H.Y., Chappell, L.J., Huff, J.L., 2013. How safe is safe enough? radiation risk for a human mission to Mars. PLoS One 8, e74988. doi:10.1371/journal.pone.0074988.

Cummings, A., Stone, E., 1996. Composition of anomalous cosmic rays and implications for the heliosphere. Space Science Reviews 78, 117–128. doi:10.1007/BF00170798.

De Angelis, G., Wilson, J., Clowdsley, M., Qualls, G., Singleterry, R., 2006. Modeling of the martian environment for radiation analysis. Radiation measurements 41, 1097–1102. doi:10.1016/j.nuclphysbbs.2006.12.035.

Desai, M., Giacalone, J., 2016. Large gradual solar energetic particle events. Living Reviews in Solar Physics 13, 3. doi:10.1007/s41116-016-0002-5.

Dobynde, M., Effenberger, F., Kartashov, D., Shprits, Y.Y., Shurshakov, V., 2019. Ray-tracing simulation of the radiation dose distribution on the surface of the spherical phantom of the matroskhar experiment onboard the iss. Life sciences in space research 21, 65–72. doi:10.1016/j.lssr.2019.04.001.

Dobynde, M., Guo, J., 2024. Guidelines for radiation-safe human activities on the moon. Nature Astronomy 8, 991–999. doi:10.1038/s41550-024-02287-8.

Dobynde, M., Shprits, Y., Drozdov, A.Y., Hoffman, J., Li, J., 2021. Beating 1 sievert: Optimal radiation shielding of astronauts on a mission to mars. Space Weather 19, e2021SW002749. doi:10.1029/2021SW002749.

Dobynde, M.I., Guo, J., 2021. Radiation environment at the surface and subsurface of the moon: Model development and validation. Journal of Geophysical Research: Planets 126, e2021JE006930. doi:10.1029/2021JE006930.

Ehresmann, B., Zeitlin, C., Hassler, D.M., Wimmer-Schweingruber, R.F., Böhm, E., Böttcher, S., Brinza, D.E., Burmeister, S., Guo, J., Köhler, J., et al., 2014. Charged particle spectra obtained with the Mars Science Laboratory radiation assessment detector (MSL/RAD) on the surface of Mars. Journal of Geophysical Research: Planets 119, 468–479. doi:10.1002/2013JE004547.

Fisk, L.A., 1971. Solar modulation of galactic cosmic rays. 2. Journal of Geophysical Research 76, 221. doi:10.1029/JA076i001p00221.

Garcia-Munoz, M., Mason, G., Simpson, J., 1973. A new test for solar modulation theory: The 1972 may-july low-energy galactic cosmic-ray proton and helium spectra. Astrophysical Journal, vol. 182, p. L81 182, L81. doi:10.1086/181224.

George, S.P., Gaza, R., Matthiä, D., Laramore, D., Lehti, J., Campbell-Ricketts, T., Kroupa, M., Stoffle, N., Marsalek, K., Przybyla, B., et al., 2024. Space radiation measurements during the Artemis I lunar mission. Nature 634, 48–52. doi:10.1038/s41586-024-07927-7.

Giacalone, J., Fahr, H., Fichtner, H., Florinski, V., Heber, B., Hill, M.E., Kóta, J., Leske, R.A., Potgieter, M.S., Rankin, J.S., 2022. Anomalous cosmic rays and heliospheric energetic particles. Space Science Reviews 218, 22. doi:10.1007/s11214-022-00890-7.

Gieseler, J., Heber, B., 2016. Spatial gradients of GCR protons in the inner heliosphere derived from Ulysses COSPIN/KET and PAMELA measurements. Astronomy & Astrophysics 589, A32. doi:10.1051/0004-6361/201527972.

Gleeson, L., Axford, W., 1967. Cosmic rays in the interplanetary medium. The Astrophysical Journal 149, L115. doi:10.1086/180070.

- Gleeson, L., Axford, W., 1968. Solar modulation of galactic cosmic rays. *The Astrophysical Journal* 154, 1011. doi:10.1086/149822.
- Goorley, T., James, M., Booth, T., Brown, F., Bull, J., Cox, L., Durkee, J., Elson, J., Fensin, M., Forster, R., et al., 2012. Initial mcnp6 release overview. *Nuclear technology* 180, 298–315. doi:10.13182/NT11-135.
- Grotzinger, J.P., Crisp, J., Vasavada, A.R., Anderson, R.C., Baker, C.J., Barry, R., Blake, D.F., Conrad, P., Edgett, K.S., Ferdowski, B., Gellert, R., Gilbert, J.B., Golombek, M., Gómez-Elvira, J., Hassler, D.M., Jandura, L., Litvak, M., Mahaffy, P., Maki, J., Meyer, M., Malin, M.C., Mitrofanov, I., Simmonds, J.J., Vaniman, D., Welch, R.V., Wiens, R.C., 2012. Mars Science Laboratory mission and science investigation. *Space Science Reviews* 170, 5–56. doi:10.1007/s11214-012-9892-2.
- Guo, J., Banjac, S., Röstel, L., Terasa, J.C., Herbst, K., Heber, B., Wimmer-Schweingruber, R.F., 2019. Implementation and validation of the GEANT4/AtRIS code to model the radiation environment at Mars. *Journal of Space Weather and Space Climate* 9. doi:10.1051/swsc/2018051.
- Guo, J., Wang, B., Whitman, K., Plainaki, C., Zhao, L., Bain, H.M., Cohen, C., Dalla, S., Dumbovic, M., Janvier, M., et al., 2024. Particle radiation environment in the heliosphere: Status, limitations, and recommendations. *Advances in Space Research* doi:10.1016/j.asr.2024.03.070.
- Guo, J., Zeitlin, C., Wimmer-Schweingruber, R.F., Hassler, D.M., Ehresmann, B., Rafkin, S., Freiherr von Forstner, J.L., Khaksarighiri, S., Liu, W., Wang, Y., 2021. Radiation environment for future human exploration on the surface of mars: the current understanding based on msl/rad dose measurements. *The Astronomy and Astrophysics Review* 29, 1–81. doi:10.1007/s00159-021-00136-5.
- Hassler, D.M., Zeitlin, C., Wimmer-Schweingruber, R.F., Böttcher, S.I., Martin, C., Andrews, J., Böhm, E., Brinza, D., Bullock, M., Burmeister, S., et al., 2012. The Radiation Assessment Detector (RAD) investigation. *Space Science Reviews* 170, 503–558. doi:10.1007/s11214-012-9913-1.
- Hassler, D.M., Zeitlin, C., Wimmer-Schweingruber, R.F., Ehresmann, B., Rafkin, S., Eigenbrode, J.L., Brinza, D.E., Weigle, G., Böttcher, S.I., Böhm, E., et al., 2014. Mars's surface radiation environment measured with the Mars Science Laboratory's curiosity rover. *Science* 343, 1244797. doi:10.1126/science.1244797.
- Honig, T., Witasse, O.G., Evans, H., Nieminen, P., Kuulkers, E., Taylor, M.G., Heber, B., Guo, J., Sánchez-Cano, B., 2019. Multi-point galactic cosmic ray measurements between 1 and 4.5 au over a full solar cycle. *Annales Geophysicae* 37. doi:10.5194/angeo-37-903-2019.
- ICRP, 1992. Recommendations of the International Commission on Radiological Protection (ICRP) 1990. *European Journal of Nuclear Medicine* 19, 77–79. doi:10.1007/BF00184120.
- Jun, I., Garrett, H., Kim, W., Zheng, Y., Fung, S.F., Corti, C., Ganushkina, N., Guo, J., 2024. A review on radiation environment pathways to impacts: Radiation effects, relevant empirical environment models, and future needs. *Advances in Space Research* doi:10.1016/j.asr.2024.03.079.
- Khaksarighiri, S., Guo, J., Wimmer-Schweingruber, R., Narici, L., Lohf, H., 2020. Calculation of dose distribution in a realistic brain structure and the indication of space radiation influence on human brains. *Life Sciences in Space Research* 27, 33–48. doi:10.1016/j.lssr.2020.07.003.
- Kim, M.H.Y., Cucinotta, F.A., Nounu, H.N., Zeitlin, C., Hassler, D.M., Rafkin, S.C.R., Wimmer-Schweingruber, R.F., Ehresmann, B., Brinza, D., Böttcher, S., Böhm, E., Burmeister, S., Guo, J., Köhler, J., Martin, C., Reitz, G., Posner, A., Gómez-Elvira, J., Harri, A.M., the MSL Science Team, 2014. Comparison of martian surface ionizing radiation measurements from MSL-RAD with badhwar-O'Neill 2011/HZETRN model calculations. *Journal of Geophysical Research: Planets* 119, 1311–1321. doi:10.1002/2013JE004549.
- Kudela, K., 2009. On energetic particles in space. *Acta Physica Slovaca* 59, 537–652. doi:10.2478/v10155-010-0098-4.
- Kulesza, J.A., Adams, T.R., Armstrong, J.C., Bolding, S.R., Brown, F.B., Bull, J.S., Burke, T.P., Clark, A.R., Forster III, R.A.A., Giron, J.F., et al., 2022. MCNP® code version 6.3.0 theory & user manual. Technical Report. Los Alamos National Laboratory (LANL), Los Alamos, NM (United States). doi:10.2172/1889957.
- Li, Y., Guo, J., Khaksarighiri, S., Dobynde, M.L., Zhang, J., Liu, B., Wimmer-Schweingruber, R.F., 2023. The impact of space radiation on brains of future martian and lunar explorers. *Space Weather* 21, e2023SW003470. doi:10.1029/2023SW003470.
- Liu, W., Guo, J., Wang, Y., Slaba, T.C., 2024. A Comprehensive Comparison of Various Galactic Cosmic-Ray Models to the State-of-the-art Particle and Radiation Measurements. *The Astrophysical Journal Supplement Series* 271, 18. doi:10.3847/1538-4365/ad18ad.
- Liu, W., Guo, J., Zhang, J., Semkova, J., 2023. Modeling the Radiation Environment of Energetic Particles at Mars Orbit and a First Validation against TGO Measurements. *The Astrophysical Journal* 949, 77. doi:10.3847/1538-4357/acce3c.
- Looper, M., Mazur, J., Blake, J., Spence, H.E., Schwadron, N.A., Golightly, M., Case, A., Kasper, J., Townsend, L., 2013. The radiation environment near the lunar surface: Crater observations and geant4 simulations. *Space Weather* 11, 142–152. doi:10.1002/swe.20034.
- Lyu, D., Qin, G., Shen, Z.N., 2024. Long-Term Variation of the Galactic Cosmic Ray Radiation Dose Rates. *Space Weather* 22, e2023SW003804. doi:10.1029/2023SW003804.
- Marquardt, J., Heber, B., Potgieter, M., Strauss, R., 2018. Energy spectra of carbon and oxygen with helios e6-radial gradients of anomalous cosmic ray oxygen within 1 au. *Astronomy & Astrophysics* 610, A42. doi:10.1051/0004-6361/201731490.
- Matthiä, D., Berger, T., 2017. The radiation environment on the surface of Mars—numerical calculations of the galactic component with GEANT4/planetocosmics. *Life sciences in space research* 14, 57–63. doi:10.1016/j.lssr.2017.03.005.
- Matthiä, D., Ehresmann, B., Lohf, H., Köhler, J., Zeitlin, C., Appel, J., Sato, T., Slaba, T., Martin, C., Berger, T., et al., 2016. The martian surface radiation environment—a comparison of models and MSL/RAD measurements. *Journal of Space Weather and Space Climate* 6, 1–17. doi:10.1051/swsc/2016008.
- Mazur, J., Crain, W., Looper, M., Mabry, D., Blake, J., Case, A., Golightly, M., Kasper, J., Spence, H.E., 2011. New measurements of total ionizing dose in the lunar environment. *Space Weather* 9. doi:10.1029/2010SW000641.
- McDonald, F., Teegarden, B., Trainor, J., Webber, W., 1974. The anomalous abundance of cosmic-ray nitrogen and oxygen nuclei at low energies. *The Astrophysical Journal* 187, L105. doi:10.1086/181407.
- Mitrofanov, I., Malakhov, A., Bakhtin, B., Golovin, D., Kozyrev, A., Litvak, M., Mokrousov, M., Sanin, A., Tretyakov, V., Vostrukhin, A., Anikin, A., Zelenyi, L.M., Semkova, J., Malchev, S., Tomov, B., Matviichuk, Y., Dimitrov, P., Koleva, R., Dachev, T., Krastev, K., Shvetsov, V., Timoshenko, G., Bobrovniksky, Y., Tomilina, T., Benghin, V., Shurshakov, V., 2018. Fine Resolution Epithermal Neutron Detector (FRIEND) Onboard the ExoMars Trace Gas Orbiter. *Space Science Reviews* 214, 86. doi:10.1007/s11214-018-0522-5.
- Naito, M., Kodaira, S., 2022. Considerations for practical dose equivalent assessment of space radiation and exposure risk reduction in deep space. *Scientific Reports* 12, 13617. doi:10.1038/s41598-022-17079-1.

- Naito, M., Kodaira, S., 2025. Charge-weighted quality factors based on let for practical dose assessment of space radiation. *Life Sciences in Space Research* doi:10.1016/j.lssr.2025.10.002.
- Niita, K., Sato, T., Iwase, H., Nose, H., Nakashima, H., Sihver, L., 2006. Phits—a particle and heavy ion transport code system. *Radiation measurements* 41, 1080–1090. doi:10.1016/j.radmeas.2006.07.013.
- Norbury, J.W., Slaba, T.C., Aghara, S., Badavi, F.F., Blattnig, S.R., Cloudsley, M.S., Heilbronn, L.H., Lee, K., Maung, K.M., Mertens, C.J., et al., 2019. Advances in space radiation physics and transport at nasa. *Life Sciences in Space Research* 22, 98–124. doi:10.1016/j.lssr.2019.07.003.
- Parker, E.N., 1965. The passage of energetic charged particles through interplanetary space. *Planetary and Space Science* 13, 9–49. doi:10.1016/0032-0633(65)90131-5.
- Potgieter, M., 2013. Cosmic rays in the inner heliosphere: Insights from observations, theory and models. *Space Science Reviews* 176, 165–176. doi:10.1007/s11214-011-9750-7.
- Rahmanian, S., Slaba, T., Braby, L., Santa Maria, S., Bhattacharya, S., Straume, T., 2023. Galactic cosmic ray environment predictions for the nasa biosentinel mission. *Life Sciences in Space Research* 38, 19–28. doi:10.1016/j.lssr.2023.05.001.
- Rahmanian, S., Slaba, T.C., George, S., Braby, L.A., Bhattacharya, S., Straume, T., Santa Maria, S.R., 2024. Galactic cosmic ray environment predictions for the nasa biosentinel mission, part 2: Post-mission validation. *Life Sciences in Space Research* doi:10.1016/j.lssr.2024.10.006.
- Rankin, J., McComas, D., Leske, R., Christian, E., Cohen, C., Cummings, A., Joyce, C., Labrador, A., Mewaldt, R., Posner, A., et al., 2021. First observations of anomalous cosmic rays in to 36 solar radii. *The Astrophysical Journal* 912, 139. doi:10.3847/1538-4357/abec7e.
- Rankin, J.S., McComas, D.J., Leske, R.A., Christian, E.R., Cohen, C., Cummings, A.C., Joyce, C.J., Labrador, A.W., Mewaldt, R.A., Schwadron, N.A., et al., 2022. Anomalous cosmic-ray oxygen observations into 0.1 au. *The Astrophysical Journal* 925, 9. doi:10.3847/1538-4357/ac348f.
- Reames, D.V., 2013. The Two Sources of Solar Energetic Particles. *Space Science Reviews* 175, 53–92. doi:10.1007/s11214-013-9958-9.
- Ricco, A.J., Santa Maria, S.R., Hanel, R.P., Bhattacharya, S., 2020. BioSentinel: A 6U nanosatellite for deep-space biological science. *IEEE Aerospace and Electronic Systems Magazine* 35, 6–18. doi:10.1109/MAES.2019.2953760.
- Röstel, L., Guo, J., Banjac, S., Wimmer-Schweingruber, R.F., Heber, B., 2020. Subsurface radiation environment of Mars and its implication for shielding protection of future habitats. *Journal of Geophysical Research: Planets* 125, e2019JE006246. doi:10.1029/2019JE006246.
- Roussos, E., Dialynas, K., Krupp, N., Kollmann, P., Paranicas, C., Roelof, E.C., Yuan, C., Mitchell, D.G., Krimigis, S.M., 2020. Long- and short-term variability of galactic cosmic-ray radial intensity gradients between 1 and 9.5 au: Observations by cassini, BESS, BESS-polar, PAMELA, and AMS-02. *The Astrophysical Journal* 904, 165. doi:10.3847/1538-4357/abc346.
- Sato, T., Iwamoto, Y., Hashimoto, S., Ogawa, T., Furuta, T., Abe, S.i., Kai, T., Tsai, P.E., Matsuda, N., Iwase, H., et al., 2018. Features of particle and heavy ion transport code system (phits) version 3.02. *Journal of Nuclear Science and Technology* 55, 684–690. doi:10.1080/00223131.2017.1419890.
- Schwadron, N.A., Baker, T., Blake, B., Case, A.W., Cooper, J.F., Golithly, M., Jordan, A., Joyce, C., Kasper, J., Kozarev, K., Mislinski, J., Mazur, J., Posner, A., Rother, O., Smith, S., Spence, H.E., Townsend, L.W., Wilson, J., Zeitlin, C., 2012. Lunar radiation environment and space weathering from the Cosmic Ray Telescope for the Effects of Radiation (CRaTER). *Journal of Geophysical Research: Planets* 117, E00H13. doi:10.1029/2011JE003978.
- Schwadron, N.A., Blake, J.B., Case, A.W., Joyce, C.J., Kasper, J., Mazur, J., Petro, N., Quinn, M., Porter, J.A., Smith, C.W., Smith, S., Spence, H.E., Townsend, L.W., Turner, R., Wilson, J.K., Zeitlin, C., 2014. Does the worsening galactic cosmic radiation environment observed by CRaTER preclude future manned deep space exploration? *Space Weather* 12, 622–632. doi:10.1002/2014SW001084.
- Semkova, J., Benghin, V., Guo, J., Zhang, J., Da Pieve, F., Krastev, K., Matviichuk, Y., Tomov, B., Shurshakov, V., Drobyshev, S., et al., 2023a. Comparison of the particle flux measured by liulinmo dosimeter in exomars tgo science orbit with those calculated by models. *Life Sciences in Space Research* 39, 119–130. doi:10.1016/j.lssr.2022.08.007.
- Semkova, J., Dachev, T., Maltchev, S., Tomov, B., Matviichuk, Y., Dimitrov, P., Koleva, R., Mitrofanov, I., Malakhov, A., Mokrousov, M., et al., 2015. Radiation environment investigations during exomars missions to mars—objectives, experiments and instrumentation. *Comptes rendus de l'Académie bulgare des Sciences* 68.
- Semkova, J., Koleva, R., Benghin, V., Dachev, T., Matviichuk, Y., Tomov, B., Krastev, K., Maltchev, S., Dimitrov, P., Bankov, N., et al., 2021. Results from radiation environment measurements aboard ExoMars Trace Gas Orbiter in Mars science orbit in May 2018–December 2019. *Icarus* 361, 114264. doi:10.1016/j.icarus.2020.114264.
- Semkova, J., Koleva, R., Benghin, V., Dachev, T., Matviichuk, Y., Tomov, B., Krastev, K., Maltchev, S., Dimitrov, P., Mitrofanov, I., Malahov, A., Golovin, D., Mokrousov, M., Sanin, A., Litvak, M., Kozlyev, A., Tretyakov, V., Nikiforov, S., Vostrukhin, A., Fedosov, F., Grebennikova, N., Zelenyi, L., Shurshakov, V., Drobyshev, S., 2018. Charged particles radiation measurements with Liulin-MO dosimeter of FRENDO instrument aboard ExoMars Trace Gas Orbiter during the transit and in high elliptic Mars orbit. *Icarus* 303, 53–66. doi:10.1016/j.icarus.2017.12.034.
- Semkova, J., Koleva, R., Benghin, V., Krastev, K., Matviichuk, Y., Tomov, B., Maltchev, S., Dachev, T., Bankov, N., Mitrofanov, I., et al., 2023b. Observation of the radiation environment and solar energetic particle events in mars orbit in may 2018–june 2022. *Life Sciences in Space Research* doi:10.1016/j.lssr.2023.03.006.
- SILSO World Data Center, 2006–2022. The International Sunspot Number. International Sunspot Number Monthly Bulletin and online catalogue URL: <http://www.sidc.be/silso/>.
- Simonsen, L.C., Slaba, T.C., Guida, P., Rusek, A., 2020. Nasa's first ground-based galactic cosmic ray simulator: Enabling a new era in space radiobiology research. *PLoS biology* 18, e3000669. doi:10.1371/journal.pbio.3000669.
- Simpson, J., 1983. Elemental and isotopic composition of the galactic cosmic rays. *Annual Review of Nuclear and Particle Science* 33, 323–382. doi:10.1146/annurev.ns.33.120183.001543.
- Slaba, T.C., Bahadori, A.A., Reddell, B.D., Singletary, R.C., Cloudsley, M.S., Blattnig, S.R., 2017. Optimal shielding thickness for galactic cosmic ray environments. *Life Sciences in space research* 12, 1–15. doi:10.1016/j.lssr.2016.12.003.
- Slaba, T.C., Blattnig, S.R., Badavi, F.F., 2010. Faster and more accurate transport procedures for HZETRN. *Journal of Computational Physics* 229, 9397–9417. doi:10.1016/j.jcp.2010.09.010.
- Slaba, T.C., Whitman, K., 2020. The Badhwar-O'Neill 2020 GCR Model. *Space Weather* 18, e2020SW002456. doi:10.1029/2020SW002456.
- Smith, M., Craig, D., Herrmann, N., Mahoney, E., Krezel, J., McIntyre, N., Goodliff, K., 2020. The artemis program: an overview of nasa's activities to return humans to the moon, in: 2020 IEEE aerospace conference, IEEE. pp. 1–10. doi:10.1109/

- AER047225. 2020.9172323.
- Spence, H.E., Case, A., Golightly, M., Heine, T., Larsen, B., Blake, J., Caranza, P., Crain, W., George, J., Lalic, M., et al., 2010. Crater: The cosmic ray telescope for the effects of radiation experiment on the lunar reconnaissance orbiter mission. *Space science reviews* 150, 243–284. doi:10.1007/s11214-009-9584-8.
- Stone, E., Frandsen, A., Mewaldt, R., Christian, E., Margolies, D., Ormes, J., Snow, F., 1998a. The advanced composition explorer. *Space Science Reviews* 86, 1–22. doi:10.1023/A:1005082526237.
- Stone, E.C., Cohen, C.M.S., Cook, W.R., Cummings, A.C., Gauld, B., Kecman, B., Leske, R.A., Mewaldt, R.A., Thayer, M.R., Dougherty, B.L., Grumm, R.L., Milliken, B.D., Radocinski, R.G., Wiedenbeck, M.E., Christian, E.R., Shuman, S., Trexel, H., Von Rosenvinge, T.T., Binns, W.R., Crary, D.J., Dowkontt, P., Epstein, J., Hink, P.L., Klarmann, J., Lijowski, M., Olevitch, M.A., 1998b. The Cosmic-Ray Isotope Spectrometer for the Advanced Composition Explorer. Springer, Dordrecht. doi:10.1007/978-94-011-4762-0_14.
- Tylka, A.J., Adams, J.H., Boberg, P.R., Brownstein, B., Dietrich, W.F., Flueckiger, E.O., Petersen, E.L., Shea, M.A., Smart, D.F., Smith, E.C., 1997. Creme96: A revision of the cosmic ray effects on micro-electronics code. *IEEE Transactions on Nuclear Science* 44, 2150–2160. doi:10.1109/23.659030.
- Vago, J., Witasse, O., Svedhem, H., Baglioni, P., Haldemann, A., Gianfiglio, G., Blancquaert, T., McCoy, D., De Groot, R., 2015. Esa exomars program: the next step in exploring mars. *Solar System Research* 49, 518–528. doi:10.1134/S0038094615070199.
- Vondrak, R., Keller, J., Chin, G., Garvin, J., 2010. Lunar Reconnaissance Orbiter (LRO): Observations for lunar exploration and science. *Space science reviews* 150, 7–22. doi:10.1007/s11214-010-9631-5.
- Vos, E., Potgieter, M., 2016. Global gradients for cosmic-ray protons in the heliosphere during the solar minimum of cycle 23/24. *Solar Physics* 291, 2181–2195. doi:10.1007/s11207-016-0945-7.
- Wilson, J.W., Slaba, T.C., Badavi, F.F., Reddell, B.D., Bahadori, A.A., 2014. Advances in nasa radiation transport research: 3dHZETRN. *Life Sciences in Space Research* 2, 6–22. doi:10.1016/j.lssr.2014.05.003.
- Wilson, J.W., Townsend, L.W., Schimmerling, W.S., Khandelwal, G.S., Khan, F.S., Nealy, J.E., Cucinotta, F.A., Simonsen, L.C., Shinn, J.L., Norbury, J.W., 1991. Transport methods and interactions for space radiations. NASA RP 1257. URL: <https://spaceradiation.larc.nasa.gov/nasapapers/RP1257.pdf>.
- Wimmer-Schweingruber, R.F., Yu, J., Böttcher, S.I., Zhang, S., Burmeister, S., Lohf, H., Guo, J., Xu, Z., Schuster, B., Seimetz, L., et al., 2020. The Lunar Lander Neutron and Dosimetry (LND) Experiment on Chang'E 4. *Space Science Reviews* 216, 1–40. doi:10.1007/s11214-020-00725-3.
- Xu, Z., Guo, J., Wimmer-Schweingruber, R.F., Dobynde, M.I., Kühl, P., Khaksarighiri, S., Zhang, S., 2022. Primary and albedo protons detected by the lunar lander neutron and dosimetry experiment on the lunar farside. *Frontiers in Astronomy and Space Sciences* 9. doi:10.3389/fspas.2022.974946.
- Zaman, F., Townsend, L., de Wet, W., Looper, M., Brittingham, J., Burahmah, N., Spence, H., Schwadron, N., Smith, S., 2022. Modeling the lunar radiation environment: A comparison among FLUKA, Geant4, HETC-HEDS, MCNP6, and PHITS. *Space Weather* 20, e2021SW002895. doi:10.1029/2021SW002895.
- Zaman, F., Townsend, L.W., de Wet, W.C., Schwadron, N.A., Spence, H.E., Wilson, J.K., Jordan, A.P., Smith, S.S., Looper, M.D., 2020. Absorbed doses from gcr and albedo particles emitted by the lunar surface. *Acta Astronautica* 175, 185–189. doi:10.1016/j.actaastro.2020.05.040.
- Zeitlin, C., Case, A., Spence, H.E., Schwadron, N.A., Golightly, M., Wilson, J.K., Kasper, J., Blake, J., Looper, M., Mazur, J., et al., 2013a. Measurements of galactic cosmic ray shielding with the crater instrument. *Space Weather* 11, 284–296. doi:10.1002/swe.20043.
- Zeitlin, C., Case, A.W., Schwadron, N.A., Spence, H.E., Mazur, J.E., Joyce, C.J., Looper, M.D., Jordan, A., Rios, R.R., Townsend, L.W., Kasper, J.C., Blake, J.B., Smith, S., Wilson, J., Iwata, Y., 2016. Solar modulation of the deep space galactic cosmic ray lineal energy spectrum measured by CRA TER, 2009–2014. *Space Weather* 14, 247–258. doi:10.1002/2015SW001314.
- Zeitlin, C., Hassler, D., Ehresmann, B., Rafkin, S., Guo, J., Wimmer-Schweingruber, R.F., Berger, T., Matthiä, D., 2019. Measurements of radiation quality factor on Mars with the Mars Science Laboratory Radiation Assessment Detector. *Life Sciences in Space Research* 22, 89–97. doi:10.1016/j.lssr.2019.07.010.
- Zeitlin, C., Hassler, D.M., Cucinotta, F.A., Ehresmann, B., Wimmer-Schweingruber, R.F., Brinza, D.E., Kang, S., Weigle, G., Böttcher, S., Böhm, E., Burmeister, S., Guo, J., Köhler, J., Martin, C., Posner, A., Rafkin, S., Reitz, G., 2013b. Measurements of Energetic Particle Radiation in Transit to Mars on the Mars Science Laboratory. *Science* 340, 1080–1084. doi:10.1126/science.1235989.
- Zhang, J., Guo, J., Dobynde, M.I., Wang, Y., Wimmer-Schweingruber, R.F., 2022. From the Top of Martian Olympus to Deep Craters and Beneath: Mars Radiation Environment Under Different Atmospheric and Regolith Depths. *Journal of Geophysical Research: Planets* 127, e2021JE007157. doi:10.1029/2021JE007157.
- Zhang, S., Wimmer-Schweingruber, R.F., Yu, J., Wang, C., Fu, Q., Zou, Y., Sun, Y., Wang, C., Hou, D., Böttcher, S.I., et al., 2020. First measurements of the radiation dose on the lunar surface. *Science Advances* 6, eaaz1334. doi:10.1126/sciadv.aaz1334.
- Zheng, Y., Ganushkina, N.Y., Jiggins, P., Jun, I., Meier, M., Minow, J.L., O'Brien, T.P., Pitchford, D., Shprits, Y., Tobiska, W.K., et al., 2019. Space radiation and plasma effects on satellites and aviation: Quantities and metrics for tracking performance of space weather environment models. *Space Weather* 17, 1384–1403. doi:10.1029/2018SW002042.